Master's Thesis : XRF instrument power supply

Auteur : Levaux, Nicolas
Promoteur(s) : Redouté, Jean-Michel
Faculté : Faculté des Sciences appliquées
Diplôme : Master : ingénieur civil électricien, à finalité spécialisée en "electronic systems and devices"
Année académique : 2019-2020
URI/URL : http://hdl.handle.net/2268.2/9038

XRF instrument power supply

Design and simulations of a qualified space model in order to perform a lunar mission for the European Space Agency (ESA)

Nicolas Levaux

Graduation Studies conducted under the supervision of
Prof. Dr. Ir. Jean-Michel Redouté

the co-supervision of
Dr. Alain Carapelle

for obtaining the Master's degree of
Science in Electrical Engineering
major in Electronic Systems and Devices

at the University of Liège - Faculty of Applied Sciences

Academic year
2019 – 2020

Title: XRF instrument power supply

Author: Nicolas Levaux
Master of Science in Electrical Engineering – major in Electronic Systems and Devices
Academic year: 2019 – 2020
Promotors: Prof. Dr. Ir. Jean-Michel Redouté & Dr. Alain Carapelle

Abstract

This thesis brings a complete redesign to the power supply of an X-Ray fluorescence (XRF) spectrometer.

XRF is the phenomenon in which an atom absorbs an X-radiation with a certain energy level and release another X-radiation with another energy level. Indeed, if the excitation source has enough energy, ionization can occur in the material and the atoms become unstable. To restore equilibrium, electrons from higher orbitals can fall to fill the gap by releasing energy (in the form of a photon) equal to the difference between the 2 orbitals involved. In an energy-dispersive spectrometer (EDXRF), the number and the energy of the incoming X-rays are measured and then sorted. A complete spectrum of the target can be obtained, and the atomic composition of the target determined.

The ALEXIS instrument is basically composed of 6 excitation sources, 1 detector and signal processing electronics. The excitation sources are pyroelectric crystals which are thermally cycled in order to have a continuous flux of X-Rays. The detector is a Silicon Drift Detector (SDD) which the actual state of art in EDXRF analysis. This technology needs to be cooled down by a Peltier element and must be polarized by a high negative voltage to drift the electron-hole pairs produced by the X-Rays impact to the collection electrode.

The first part of the thesis is dedicated to the design of a controller for a current source driving the Peltier cooler. The goal is to obtain a stable cold temperature of the detector chip during the measurements. In space applications, due to radiations, analog electronics is preferred to digital. That is why an analog PID controller has been implemented based on the temperature feedback coming from the SDD. The finality of this part is a series of simulations to tune PID parameters.

The second part of the work is the implementation of the thermal cycle of the sources. Two temperature thresholds determine if the source must be powered up or not and the 6 sources must work independently. In order to achieve this, an analog Schmitt trigger was designed on each source with a digitally controlled gain attenuator to control the output voltage. Final simulations give results very close to the real lab tests.

The last part of the project described the method to design a DCM Flyback converter. The goal is to generate negative high voltage from the rover power supply (28V) in order to generate the drift electric field in the SDD. A spreadsheet was created. It automatically computes the circuit parameters according to the input/output requirements. The conclusion is open-loop simulations performed to show the influence of the parameters. Future closed-loop design is just discussed.

Keywords: EDXRF, ALEXIS project, power supply, Peltier cooling, analog PID controller, Schmitt trigger, DCM Flyback converter.

Preface

"Pour tirer le meilleur parti des connaissances acquises, pour en extraire toute la richesse, il importe de ne pas s'y habituer trop vite, de se laisser le temps de la surprise et de l'étonnement."

- Hubert Reeves, astrophysicist

This master thesis is the culmination of my University course. It was written to fulfill the requirements for obtaining the diploma from the Faculty of Applied Science at the University of Liège. I present this thesis in order to obtain the Master's degree of Science in Electrical Engineering (major in Electronic Systems and Devices).

The master thesis "XRF instrument power supply" is presented to you in accordance with the knowledge accumulated during my university training. The Master's in Electrical Engineering enabled me to use this knowledge and to understand the foundations of electricity, electronics and IT to harness, analyse, transform and transmit information and energy.

The project was undertaken in collaboration with the Centre Spatial de Liège, a research center where I did my internship. This work takes place in a 20 year XRF development in CSL. My research subject - the power supply - was established in collaboration with my internship supervisor, Alain Carapelle.

Acknowledgements

First of all, I would like to thank Alain Carapelle, who gives me the opportunity to work on this space project at CSL. He succeeds to transmit me a piece of his passion for radiations and for space missions in general. I'm grateful for his follow-up and his high reactivity during the whole period even when a sanitary crisis happens and forces home-working.

Then, I would like to thank Professor Jean-Michel Redouté, my academic supervisor, who knew how to find the encouraging words to motivate me to adapt my work in these particular conditions that the COVID-19 crisis imposed. His kind and enthusiast feedback has been really important for the progress of this thesis.

Of course, I do not forget to thank my electronic referrer, Jean-Marie Gillis, who is a real source of knowledge in the field of electronics and to the whole team from the electronics lab at CSL, headed by Nicolas Martin, for their availability and their help when needed.

Finally, I would like to thank my family and friends for the support they brought to me, not only for this thesis, but also during these five years of studies punctuated by this work.

Table of Contents

List of Figures

List of Abbreviations

A	Ampere, Area or Amplifying term
A/D	Analog to Digital
ALEXIS	A Lunar Experiment of X-ray Induced Spectroscopy
ASIC	Application-Specific Integrated Circuit
B	Low (Bas in french) or flux density
b	base
C	Capacitor, Capacitance or Celsius
c	collector
CCD	Charge-Coupled Device
CCM	Continuous Conduction Mode
CLS	Coarse Lateral Sensor
CMOS	Complementary Metal Oxide Semi-conductor
COPERS	Commission Provisoire d'Etudes et de Recherches Spatiales
CSL	Centre Spatial de Liège
Cu	Copper
D	Diode, Duty cycle or Density
d	derivative
DC	Direct Current
DCM	Discontinuous Conduction Mode
ds	drain-source
dT	difference of Temperature
e	emitter or effective
EDS	Energy Dispersive Spectroscopy
EDXRF	Energy Dispersive X-Ray Fluorescence
EMC	ElectroMagnetic Capability
EMI	ElectroMagnetic Interference
EPPL	European Preferred Part List
err	error
ESA	European Space Agency
ESCC	European Space Components Coordination
ESIO	Extreme-UV solar Imager for Operations
ESRO	European Space Research Organization
ESTEC	European Space Research and Technology Centre
eV	electronvolt
F	Farad
f	frequency
Fe	Iron
fe	magnetic
FM	Flight Model
FP	Flat Package
G	Gain
g	gram or generator

GND	Ground
gs	gate-source
GSTP	General Support Technology Programme
H	Henry or High
HV	High Voltage
Hz	Hertz
I	current
i	integral
IAL	Institute of Astrophysics Liège
in	input
IT	Information Technology
J	Joule
JUICE	JUpiter ICy moons Explorer
K	Kelvin
k	kilo
KUL	KU Leuven
L	Inductor or inductance
l	length
Li	Lithium
lk	leakage
LUVMI	LUnar Volatiles Mobile Instrument
LUVMI-X	LUnar Volatiles Mobile Instrument - eXtended
m	milli, mass, magnetic, magnetizing or meter
max	maximum
min	minimum
MLT	Mean Length Turn
n	turn ratio
NASA	National Aeronautics and Space Administration
NDT	Nondestructive Testing
Ne	Neon
O	Oxygen
op-amp	operational amplifier
out	output
P	Power
p	proportional, primary or pico
P-P	Peak to Peak
PACS	Photodetector Array Camera and Spectrometer
PCB	Printed Circuit Board
PID	Proportional Integral Derivative
pk	peak
pot	potentiometer
ppm	parts per million
pr	primary
Proba-3	Project for On-Board Autonomy-3
PWM	Pulse Width Modulation
Q	heat flux
Qx	Quadrimester number x

R	Resistor
R&D	Research and Development
RMS	Root Mean Squared
s	switching, secondary, supply, snubber or second
sat	saturation
sc	secondary
SDD	Silicon Drift Detector
set	set-point
SH	Specific Heat
Si	Silicon
T	Temperature
t	time
Ta	Tantalum
TEC	Termo-Electric Cooler
temp	temperature
tot	total
trig	trigger
TRL	Technology Readiness Level
TRP	Technology Research Programme
UV	Ultra-Violet
V	Volts, Voltage or Volume
VR	Reflected Voltage
W	Watt
w	window
WDXRF	Wavelength Dispersive X-Ray Fluorescence
WP	Work Package
WRTF	Wide Range Thermal Facility
XR	X-Ray
XRF	X-Ray Fluorescence
Z	impedance

Chapter 1
Introduction

1.1 ALEXIS project

The ALEXIS (A Lunar Experiment of X-ray Induced Spectroscopy) instrument is a project led by a Belgian collaboration of several companies, universities and institutes: KU Leuven, the Royal Belgian Institute for Space Aeronomy, Mirion technologies (CANBERRA Olen), MAGICS, ULiege Geology Department, and Centre Spatial de Liège (CSL). Figure 1.1 shows these different partners and their roles.

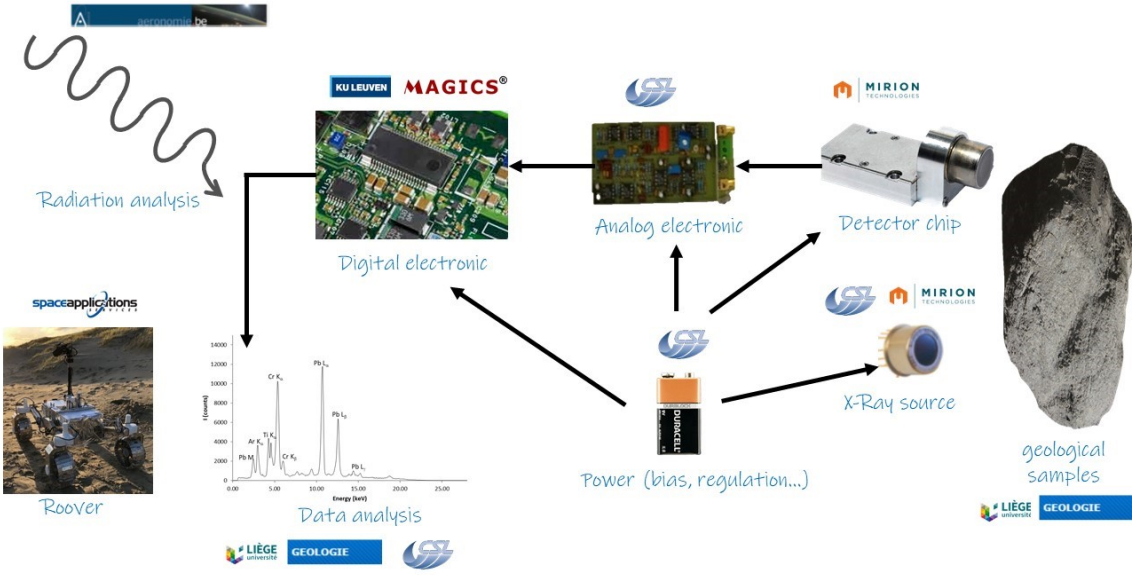

Figure 1.1 – Roles of partners

The instrument consists in a miniature X-Ray Fluorescence spectrometer that is able to identify atoms heavier than Ne. It is mainly composed of 3 parts: the detector chip, the X-ray sources and the electronics to acquire and process the data.

The goal is to design a Flight Model (FM) lighter than 500 grams using 6 sources and 1 detector chip. The disposition of these elements is illustrated in figure 1.2.

1.1.1 Emitter

Typical excitation sources are actually miniature X-Ray tubes (with a consequent power consumption of about 10 watts and a consequent weight about 400 grams) or radioisotope sources (no power consumption, a few grams weight but safety issues).

The device for this project presents an innovative source: a heated pyroelectric crystal which produces X-rays. This system permit to achieve a weight of only a few gram with an electrical consumption of less than 0.3 watts. Its size is also quite lower as shown in figure 1.3.

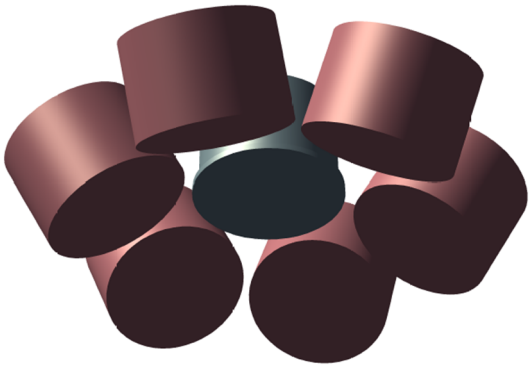

Figure 1.2 – Sources (purple) and detector (blue) configuration for FM

Figure 1.3 – Pyroelectric X-Ray source [2]

The emitter is working in pulsed mode where each pulse is produced alternatively during a heat and then a cold phase as illustrated in figure 1.4.

1.1.2 Detector

The detector is the latest generation of semi-conductor Silicon Drift Detector for X-Ray and is provided by Mirion Canberra Olen. This technology provides high resolution as low as 124 eV (measured at 5.9 keV with a ^{55}Fe source). The SXD30M-500-CM-PA model is shown in figure 1.5.

1.1.3 Signal acquisition and processing

First a CMOS pre-amplifier stage is included with the detector chip in order to amplify the signal.

Secondly, the output signal from the detector is pulse shaped by analog electronics developed in CSL. The goal is to amplify and shape the pulses of the detector in order to be compatible with the digital part. This part is studied in the frame of another master thesis for this academic year (Gary Lejeune).

Finally, the reshaped form coming from the analog stage can undergo several additional processing trough the digital electronics part. This part will be studied by the KUL.

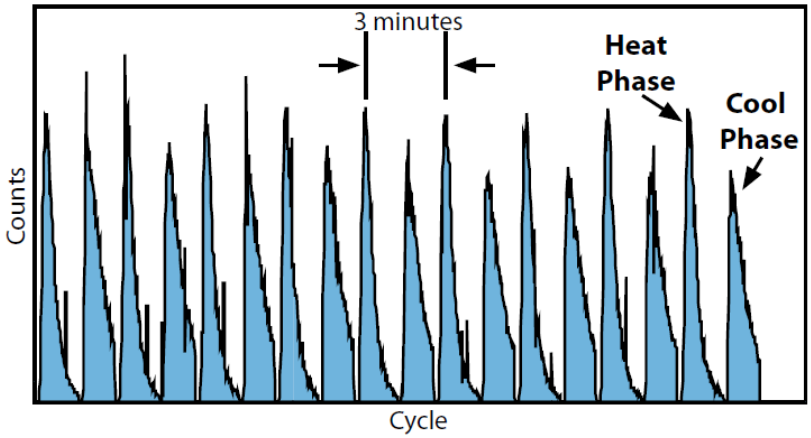

Figure 1.4 – Pyroelectric source as a function of time [2]

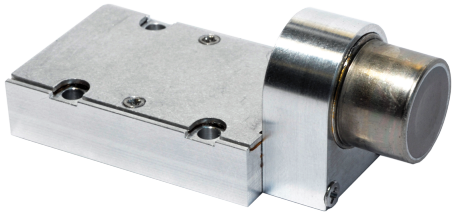

Figure 1.5 – SXD30M-500-CM-PA, SDD for X-Ray [20]

1.1.4 Objectives and steps involved in this thesis

This work takes place in a 20 year XRF development in CSL. A series of 3 generations of prototypes has been developed and preliminary tests have been performed on representative rock for the Moon. These 3 generations are shown in figures 1.6 and 1.7.

The objective of the project, involved in this thesis, is to build a Technology Readiness Level (TRL) $6 \sim 7$ engineering model of the instrument, based on available TRL 4 prototype. The goal will be to execute a vacuum functional test of the whole device including measurement on a representative sample under vacuum.

Technology Readiness Levels are a well-established standard adopted by ESA, NASA and many other agencies in order to enable discipline-independent assessments of the maturity of a particular technology and the consistent comparison of maturity between different types of technology, all in the context of a specific system, application and operating environment. The different levels are described in figure 1.8.

Luvmi-X The final prototype will be designed to be compatible with an integration on-board Luvmi X rover demonstrator in a unit cube volume. LUVMI-X is a lightweight lunar rover bound for the polar regions of the Moon. Its mission is to search for water and other volatiles, scoping out the lunar environment in support of the establishment of a lunar economy and of future human missions to the Moon and beyond.

LUVMI-X is an evolution of LUVMI rover that provides more payload accommodation and deployment capabilities, including deployment of small payloads (droppable and propellable ones), all within a lower mass and volume.

Figure 1.6 – Generation 1 and 2 prototypes [5]

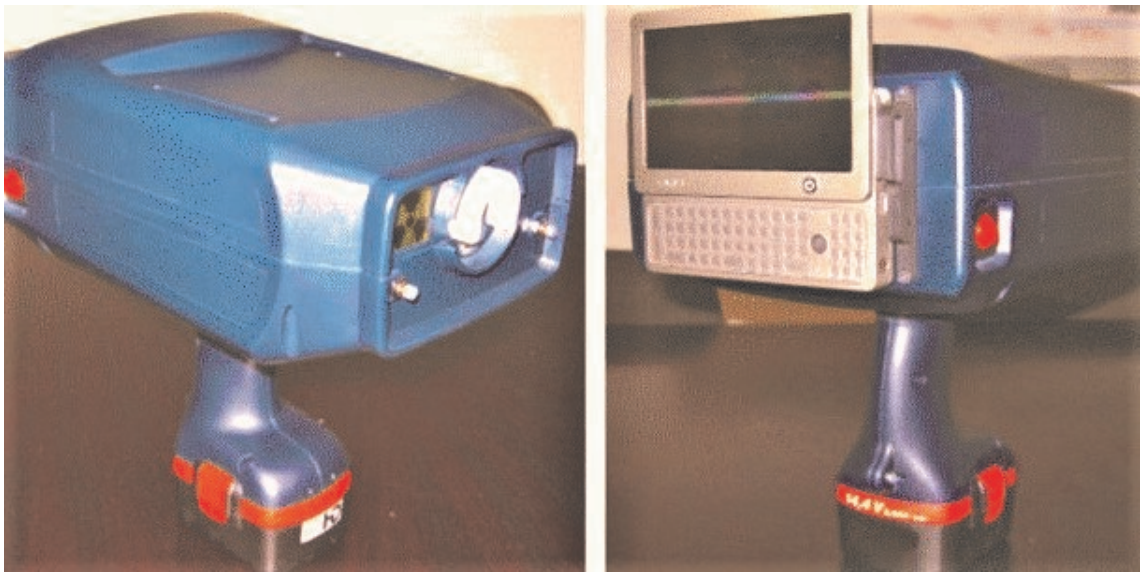

Figure 1.7 – Generation 3 prototype [6]

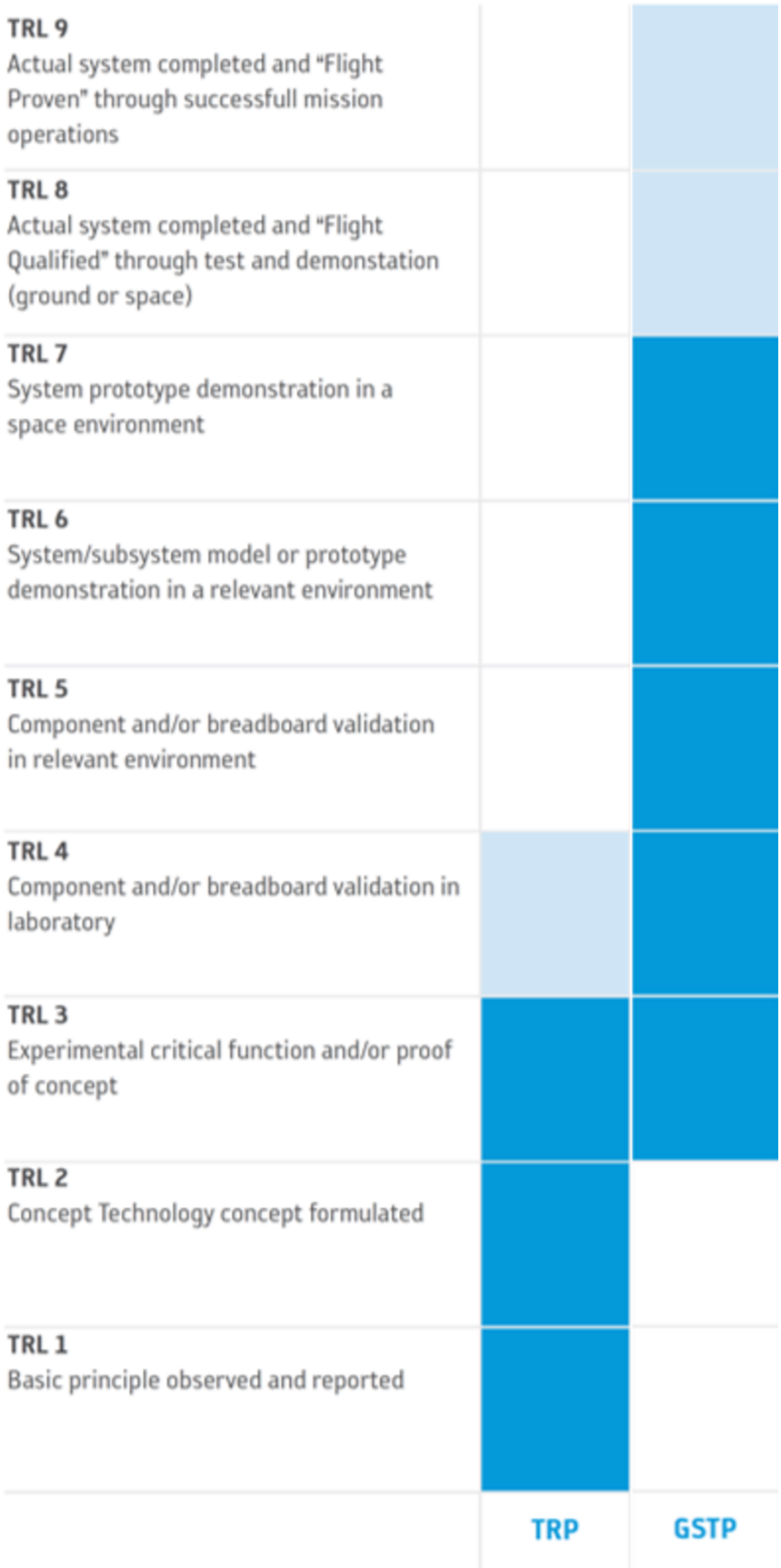

Figure 1.8 – TRL scale levels with respect to TRP (Technology Research Programme) and GSTP (General Support Technology Programme) [13]

Inputs	Detailed schematic of current shaping amplifier Analog signal simulator Datasheet of pyroelectric X-Ray generator Datasheet of SDD X-Ray detector
Tasks	Design a shaping amplifier with vacuum compatible components (preferably from space qualified family components) Design of power supply Design of pyroelectric controller PCB layout of unique board with 3 functions (amplifier, power and pyroelectric controller) Manufacturing of electronic board Testing of electronic board
Outputs	Tested electronic board with detailed schematic, PCB layout and bill of materials
Deliverables	D2: analog electronic board D2.1: analog electronic board design report

Table 1.1 – Work Package 2, Analog electronic

In Q4 2018, the LUVMI ground prototype was tested in an analogue campaign near ESTEC with different terrains and conditions, validating the platform's mobility and key aspects of the operational concept. TRL 4 equivalent was reached, although not covering thermal or avionics subsystems.

LUVMI-X team is working on design improvements for mass and performance optimization. As a highlight, they intend to validate a quarter of the locomotion train (inc. a wheel plus driving and steering motors, and adjustable suspension) in vacuum-thermal representative conditions (TRL 5+). Other subsystems will be functionally validated in the scope of the project, but their TRL maturation will take place in complementary activities which are in the process of putting in place with private and institutional partners such as this XRF project.

A maiden LUVMI-X lunar mission is expected in Q4 2024.

Work package

The overall project is structured in 13 work packages. Each package has a contractor, a duration, inputs & outputs, tasks and deliverables. This thesis is part of the WP2, "Analog electronic" contracted by the CSL. This WP is presented in Table 1.1.

Shaping amplifier is not part of this thesis and due to sanitary reasons, the work presented in this study will be limited at the design and simulation parts of the power supply (and pyroelectric controller).

1.2 Physical principles

1.2.1 X-Ray fluorescence

X-rays are an electromagnetic radiation which occurs at wavelengths ranging from 0.03 to 3 nanometers. These wavelengths correspond to an energy between 100 eV and 200 keV which can be qualified as "high-energy" radiation. X-radiation has been discovered

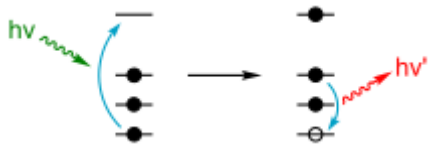

Figure 1.9 – X-Ray Fluorescence [36]

by William Rontgen in 1895 in Germany. The name given to these radiations comes from the fact that they were unknown at the time.

When exposed to such radiations, materials' components can be ionized if the X-ray energy is greater than their ionization energy. One (or more) electrons may thus be ejected from the atoms. X-rays can be energetic enough to expel tightly held electrons from the inner orbitals. The atom becomes unstable and electrons from higher orbitals fall to fill up the hole created by the ionization. The fall creates energy (in the form of a photon) equal to the difference between the 2 orbitals energy level involved (and characteristic for each atom). The fluorescence is thus the phenomenon in which an atom absorbs a radiation with a certain energy level and release another radiation with another energy level. This principle is illustrated in figure 1.9.

Each atom has electronic orbitals of characteristic energy. There are a limited number of ways in which electronic transitions can happen. When an electron in the K-shell is ejected, transition from L layer (usually called K_α) or from M layer (called K_β) can happen to fill the hole created. When a hole is created in the L shell by either the primary excitation x-ray or by the previous events, $M \rightarrow L$ transition (called L_α) can happen. However, M-L transitions and so on are possible, but their likelihoods are low. Each of these transitions yields a unique fluorescent photon with a characteristic energy related to the wavelength of the radiation by the Planck constant h:

$$\lambda = \frac{hc}{E} \tag{1.1}$$

This phenomenon is called characteristic radiation and differs for each atom type. Indeed, each element has its specific arrangement of its electrons (at discrete energy levels). The characteristic radiation depends on the binding energy of a particular element because these binding energies are different in each element.

1.2.2 Types of analysis

There are 2 ways to analyse the fluorescent radiation: sorting the photons by their energy (energy-dispersive analysis: EDXRF) or separating the wavelengths of the radiation (wavelength-dispersive analysis: WDXRF). Once sorted, the intensity of each characteristic radiation is used to identify the amount of each element in the material.

In the frame of this project, EDXRF is used with the SDD technology.

Wavelength-dispersive analysis

In order to separate the different wavelengths, the photons are diffracted by a single crystal before being detected. In order to obtain a complete spectrum, it is necessary to vary the angle of the crystal (with a precision mechanical system which move sequentially). In practice, the detector is a linear CCD. This principle is illustrated in figure 1.10.

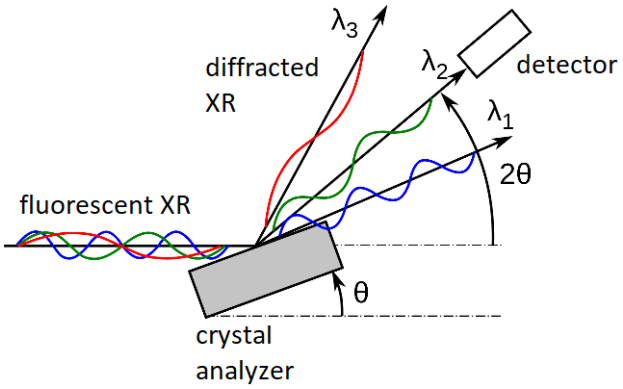

Figure 1.10 – Wavelength-dispersive analysis [36]

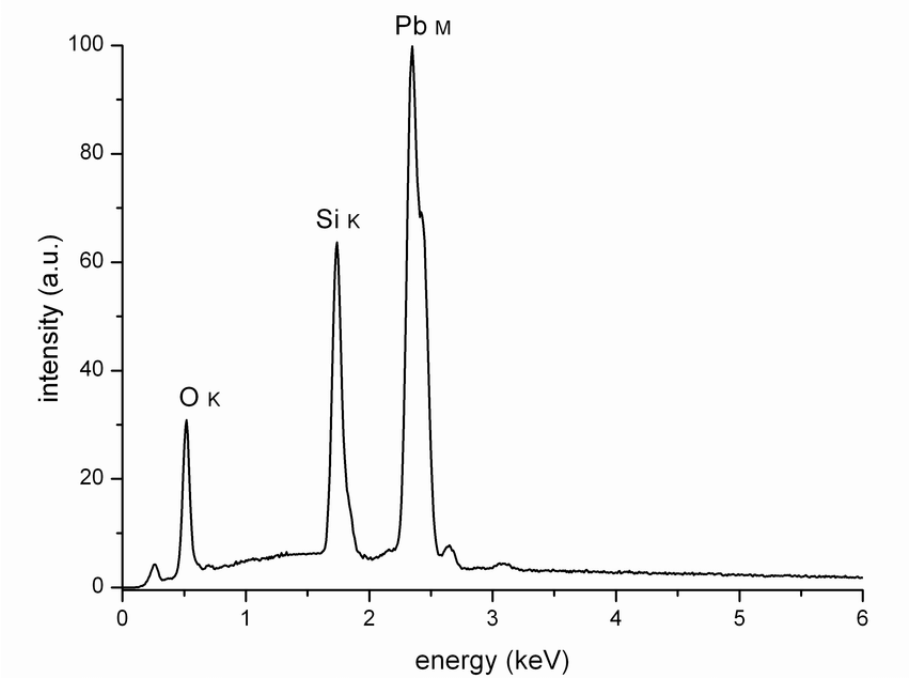

Figure 1.11 – EDS spectrum of as-prepared lead-silicate glass [17]

This type of analysis is not suitable for this application because of the mechanical system. Indeed, this system is heavy and expensive and secondly, it is not ideal to bring mechanical constraints in space.

Energy-dispersive analysis

Following the description of X-ray fluorescence, the energy level of a fluorescent X-ray is characteristic for each atom type (depending the electronic transition). In an energy-dispersive spectrometer, the number and the energy of the incoming X-rays are measured and then sorted. A complete spectrum of the target can be obtained easily as the one shown in figure 1.11.

Detector devices are usually semiconductors at solid state (Si(Li) or SDD). This semiconductor is polarized by an electric field (bias). When an incoming photon arrives on the chip, ionization is produced in the material. The electron-hole pair will then migrate under

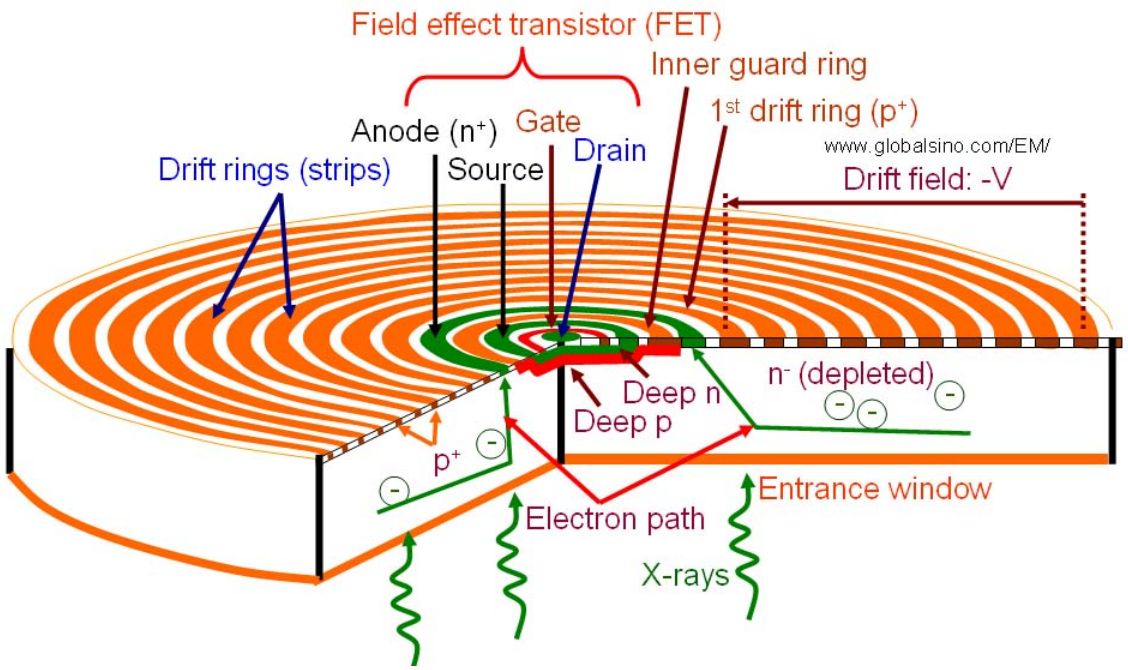

Figure 1.12 – Silicon Drift Detector [26]

the electric field and produce current pulses. These pulses have an intensity proportional to the energy of the incoming photon and thus can be sorted by energy level. The main drawback of this technique is that some element pulses are not very distinct. Indeed, the distribution of the pulses gives rays of a certain width. This distribution depends on the detector, the electronics and the temperature. Also, some pulses from other transitions can overlap and make the spectrum more complex.

Silicon Drift Detector is the actual state of the art in X-Ray energy-dispersive analysis. The material used here is high purity silicon with a very low leakage current. The drift concept come from that the transversal field is generated by a series of ring electrodes that causes charge carriers to drift to a small collection electrode. The setup is presented in figure 1.12. This anode present an extremely low capacitance (independent of the detector active area). These principles bring a series of advantage such as: high count rates & processing, better resolution at high count rates than Si(Li) detectors, lower dead time, faster analytical processing. High purity allows to be stored and operated at relatively high temperatures and allows Peltier cooling (instead of liquid nitrogen).

1.2.3 Pyroelectric crystals for X-Ray generation

Pyroelectric crystals are materials that have the capability of producing a temporary voltage when they undergo a temperature change. This heat flux changes the atom positions in the crystal structure such that a polarization appears in the material.

For X-Ray generation, the pyroelectric crystal is stick to a heater and surrounded by a low pressure gas. A metal target is also placed at the edge of the low pressure chamber, facing the Z-face of the crystal.

When the heater is switched on (heat phase), the pyroelectric crystal polarization is decreased, producing an electric field. The few electrons present in the gas chamber

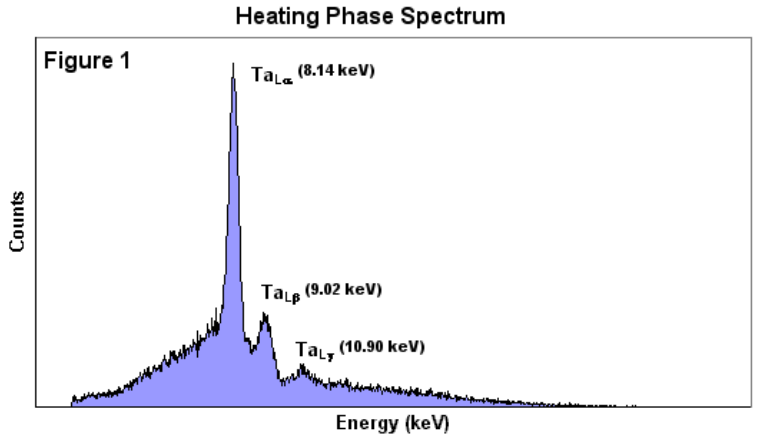

Figure 1.13 – Pyroelectric source emission spectrum during heat phase [2]

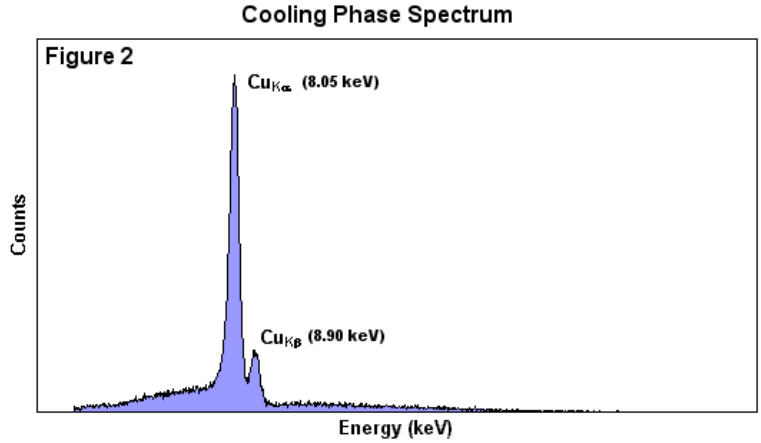

Figure 1.14 – Pyroelectric source emission spectrum during cold phase [2]

are so accelerated by this electric field towards the crystal side. These electrons interact with the gas molecule, producing more electrons (and positive charges) so that there is a multiplication of the number of electrons incident to the crystal. The results, presented in figure 1.13, are characteristic X-Rays of the elements in the crystal ($LiTaO_3$). Indeed, if electrons hit the crystal with enough energy (at or above the L-absorption edge of Ta), X-Rays are created. The slowing down on the impact will also produce the bremsstrahlung (continuum under the peaks).

When the heater is switched off (cold phase), the crystal is cooling down and its polarization increases, producing an inverse electric field (compared to heat phase). The electrons accumulated on the crystal surface are accelerated away and strike the metal target (Cu). This produces Cu K X-Rays if the electron energy is sufficient to excite the K-absorption edge in Cu. This result is presented in figure 1.14.

1.3 Power supply specification

As a first approach, this specification is describing the requirements of the power supply. This description was made at the start of the work, but was regularly updated to be

coherent with the actual design.

1.3.1 Functional description

The supply will deliver low voltages, current regulator for a Peltier module, a DC high voltage and a switchable voltage source for thermally cycling of a pyroelectric crystal controlled by a temperature sensor. An actual working circuit must be redesigned to obtain a qualifiable model which satisfied spatial conditions (vacuum compatibility, low power consumption, lightweight, electronic component space-compatible).

1.3.2 Power supply (input)

The instrument will be carried by a rover: LUVMI-X. The supply mode is a DC battery with the following voltages: 28V (most likely), 12V (certainly) and 5V (certainly).

1.3.3 List of desired output connections

- 6 X-Ray generators, COOL-X:
  - Controller system with a switchable voltage source triggered by low and high temperature points (measured by the temperature sensor): current source 1mA DC, V_{off} 0V, V_{on} 2.5V-4.5V.
- X-PIPS™detector (SDD), SXD30M-500-CM-PA:
  - Current for temperature diode bias (Peltier): 45µA.
  - TEC voltages control (Peltier) thanks to the diode (and GND) temperature: max 3.6V and 0.4A. (Operating temperature: 0°C to 50°C but gain stability: 10°C to 30°C).
  - Preamp power supplies:
    - Low voltage: +/- 5V (nominal 15mA, average 12/10mA), absolute maximum +/- 6.3V.
    - High voltage: - 225V (for detector bias).
      Ripple: 5mV P-P.
- Analog amplifier:
  - Low voltages supply: +/- 5V (according to Gary Lejeune's work).

1.3.4 User requirements

Need of independent switching on/off source, low voltages, high voltage and Peltier for the following reasons:

- avoid shutting down the detector to keep same temperature conditions between two measurements (and thus keep the same resolution).
- avoid shutting down the detector because there is a setup time (recommended by the manufacturer) independent of temperature conditions.
- permit to make "source off" measurements to get completely different data for free (Space weather on the Moon, in particular X-spectrum of precursor flashes from solar flares).

Need of a sequence to switch on the voltages for the detector. The switching off must be done in the reverse order. The thermo cooler may be switched on and off before, during and after detector operation.

1. Low voltages: +/-5V
2. High voltage: -225V

1.3.5 Product size

The whole system's weight is limited to 500 grams (power supply, emitters, detector, analog amplifier...). The system should be as small as possible with respect to a high efficiency.

1.3.6 Product environmental conditions

The product will work at temperatures between 40K and 400K, depending on the sunshine. For lab tests, a humidity rate of 50% must be taken into account, but in vacuum, there is no humidity.

1.4 Block diagram

The Figure 1.15 presents a first sketch of the relation between the different part of the system.

1.5 Structure of the document

After this first chapter of introduction, the second chapter will design an analog PID controller to regulate the Peltier cooler. Then, in chapter 3, the source generators will be implemented thanks to a design based on a Schmitt trigger. Finally, the fourth chapter will describe the open-loop design of a DCM flyback converter to produce a high negative voltage for detector bias before the last chapter as a conclusion of this work.

The end of the document is punctuated by 4 appendices: the first one is the report about the internship in CSL, the second will be a tool to choose operational amplifiers suitable for this thesis. The third one is a general schematic of the whole power supply and the last one is an excel spreadsheet to compute parameters of the DCM Flyback.

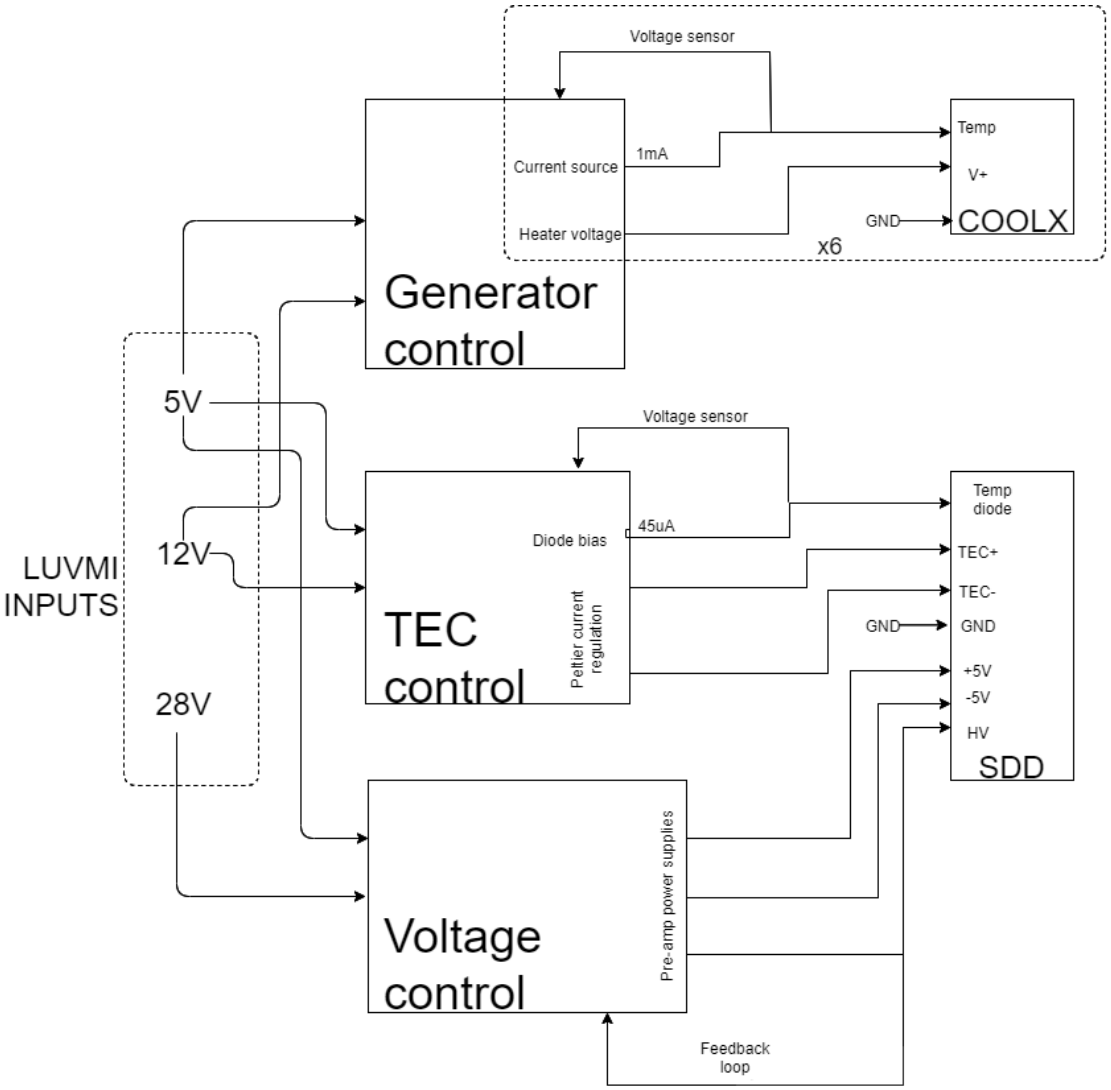

Figure 1.15 – Block diagram of the power supply

Chapter 2
Peltier cooler regulator

This second chapter is dedicated to the design and to simulations of an analog solution to control a Peltier cooler. Firstly, the conditions of operation and the frame of this cooler will be clearly defined. Then, a LTSpice model of this thermo-electric element will be built. This Peltier module is controlled by the current. That is why, in the third section, this current source will be designed and an analog PID will be implemented in order to control it. Finally, simulations will be performed to tune the PID parameters and have a desired response behaviour. The conclusion will bring some food for thought for the practical implementation.

2.1 Purpose and specifications

The detector includes a low power Peltier Cooler. In fact, the more the SDD is cooled, better performance it has. In a future thermal design, the CMOS preamplifier will be cooled in order to operate at typical temperatures within a range of ambient temperature between 10°C and 30°C. In this range, the energy resolution is guaranteed with a gain stability lower than 25 ppm/°C.

In order to have coherent measurements, the goal of the controller will be to maintain a temperature as stable as possible for the detector chip. The detector will give better performance with lower temperature. The set-point must be chosen as low as possible with respect to the Peltier limitations and environmental conditions. This point will be discussed later.

2.1.1 Data-sheet specifications

The SXD30M-500-CM-PA data-sheet gives some useful information to control the Peltier element. This one is driven by current with 2 pins, TEC+ and TEC- and gives temperatures feedback with 2 other pins, Temp. GND and Temp Diode.

The temperature diode requires a bias current of 45µA and delivers a voltage inversely proportional to the temperature of the Peltier cold surface. The relation is linear with a slope of -2.183mV/°C and a zero degree voltage of 636mV. This is illustrated in figure 2.1.

2.2 Peltier cooler model for LTSpice simulations

The Peltier element is a 2MC04-039-15/Z2 thermo-electric cooler. Owing to the data-sheet, an equivalent circuit can be modelled. The behaviour of the difference of temperature between the cold and hot plates as a function of the input current is shown in figure 2.2.

2.2.1 Electrical model

The V-I curve in figure 2.2 is linear with a slope of 9. The Peltier element can thus be modelled by a simple resistor of 9Ω directly connected to the 2 pins TEC+ and TEC-.

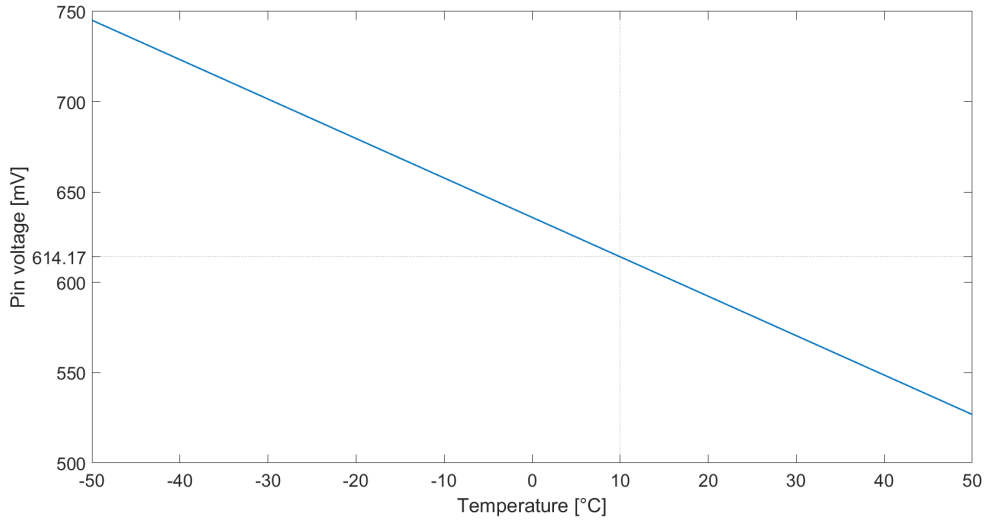

Figure 2.1 – Evolution of pin voltage with temperature

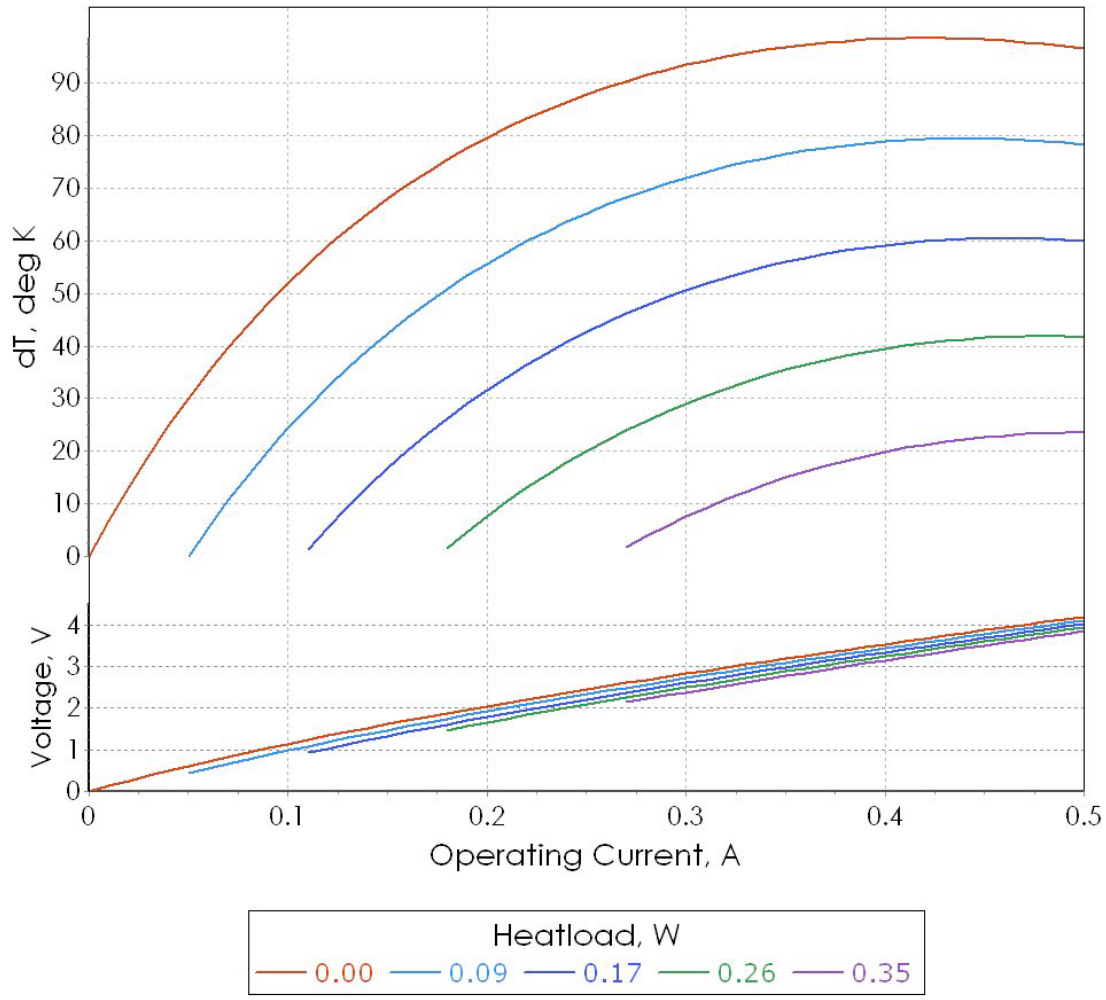

Figure 2.2 – Temperature gradient and voltage as a function of the input current [22]

Dimensions	
Length [mm]	8.0
Width [mm]	8.0
Heigth [mm]	0.5
Emmisivity	0.8
Material	Silicon
Density [kg/m^3]	2.330
Thermal conductivity [W/mK]	150
Specific heat [J/kgK]	705
Electrical conductivity [10^6/mOhm]	400.000

Table 2.1 – TECCad parameter for "Cold exchanger"

The offset induced by an input thermal flux will be assumed to be negligible.

2.2.2 Thermal model

For the thermal part, the temperature will be modelled by voltage and thermal flux by the current. So the temperature gradient will be modelled by a voltage source driven by the current passing trough the electrical resistor.

First, an approximation of the equation of the dT curve is found using Excel. Adding points every 0.1A allows to draw a trend curve. The curve becomes close to the real one (coefficient of determination $R^2 = 0.9998$) with a polynomial interpolation of third degree which correspond to this equation:

$$dT(I) = 703.7I^3 - 1181.3I^2 + 610.62I + 0.246 \tag{2.1}$$

The constant term is removed in order to keep a null behaviour with no input current.

Finally the effect of the input thermal flux must be designed. This input "current" will be sense trough a resistor of arbitrary value (10Ω) and will drive a voltage source, i.e. a temperature gradient, which will be added to the equation (2.1). A new assumption is made here: all the curves are parallel so that the offset induced by a thermal flux is linearly related to this thermal flux. Again, a linear interpolation (removing the constant term) is operated using Excel. The dT drop equation is:

$$dT_{drop} = 229.79Q_{in}(+0.0158) \tag{2.2}$$

Thermal capacitance of the detector

A capacitor is added on the cold side in order to represent the thermal capacity of the SDD. The value is calculated with respect to the data furnished by Mirion. Indeed, Mirion used a software, TECCad Lite, to generate dT curves in its data-sheet. This application takes into account a lot of different parameters. One section of the program is dedicated to the cold side and is called "Cold exchanger". The parameter from this section provided by Mirion are listed in table 2.1. In this configuration, the detector is assumed to be parallelepiped. In fact, the detector chip has an octagonal form with the same order of dimension.

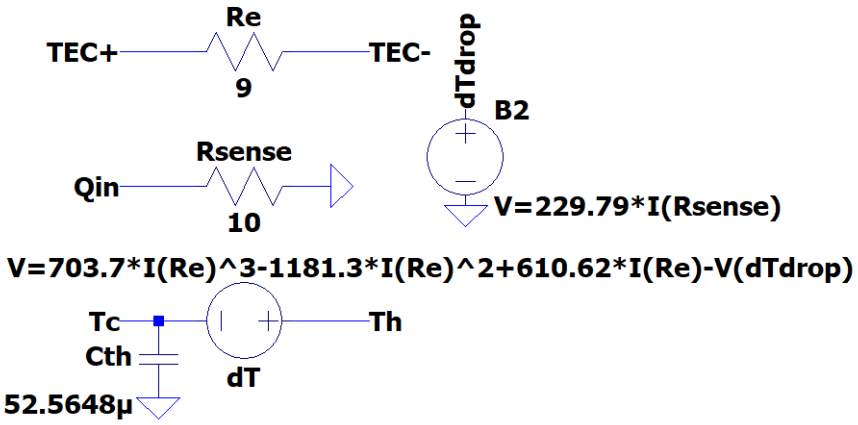

Figure 2.3 – Equivalent circuit of the Peltier cooler

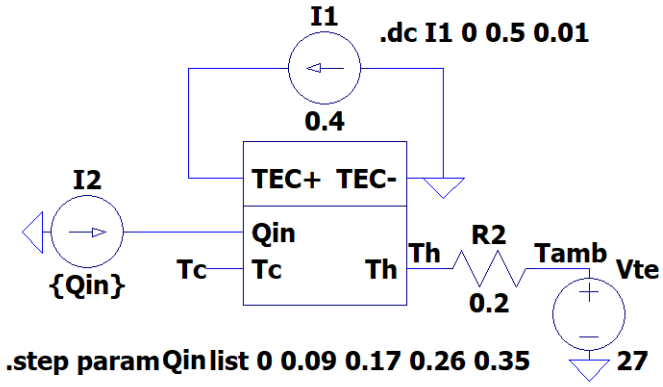

Figure 2.4 – Testing circuit of the Peltier model

The thermal capacitance is calculated following these equations:

$$V = 8.0 * 8.0 * 0.5 = 32mm^3 = 3.2 \times 10^{-8}m^3 \tag{2.3}$$

$$m = D * V = 2.330 * 3.2 \times 10^{-8} = 7.456 \times 10^{-8}kg \tag{2.4}$$

$$C = SH * m = 705 * 7.456 \times 10^{-8} = 5.25648 \times 10^{-5}J/K \tag{2.5}$$

corresponding to an electrical capacitance value of 52.5648 µF. The capacitor voltage is initialized to the ambient temperature thanks to its initial charge.

2.2.3 Equivalent circuit and first simulation

The resulting equivalent circuit is shown in figure 2.3. For simulation, the ambient temperature is fixed at 27°C at the hot side trough a thermal resistor R2 which represent the radiator. The circuit is shown in figure 2.4. The result of the simulation is shown in figure 2.5 and is very close to the real one in figure 2.2.

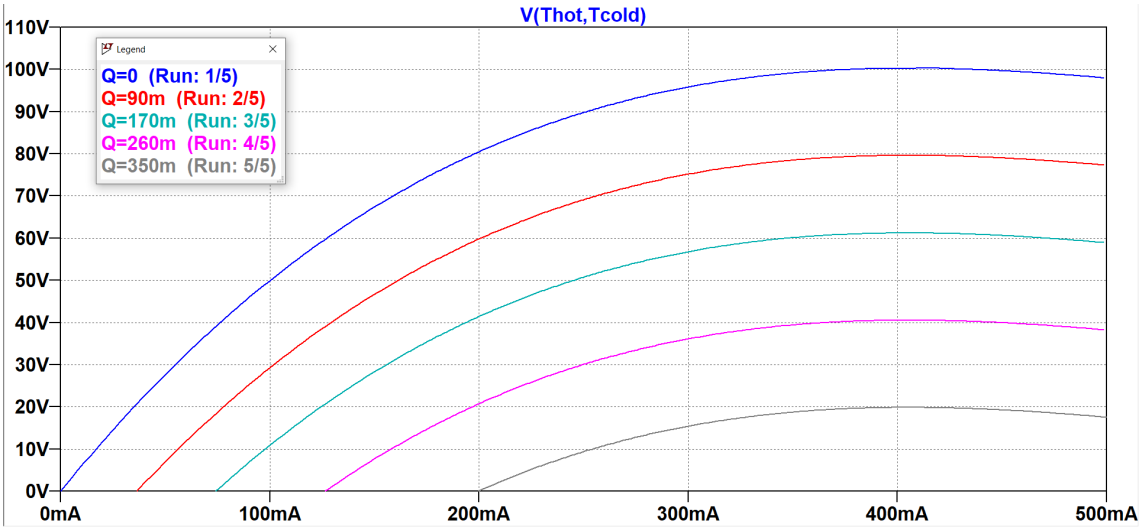

Figure 2.5 – Result of the simulation of the Peltier model (1V = 1°C)

2.3 Analog controller for a current source

The Peltier module is current driven. This current causes a heat transfer between cold and hot plate of the Peltier and thus a temperature difference. The output of the system is the temperature of the cold face. The feedback is provided thanks to the Temp. Diode pin which is a temperature/voltage conversion. The control will be done with a closed loop system.

2.3.1 Choice of topology

In a space application, analog electronics is preferred to digital. Indeed, radiations are more present than on Earth, which cause more undesired behaviour on digital signals and integrated circuit. The design must thus be thought in an analog way.

One of the actual state of the art in linear control systems is the PID controller. This technique is compatible with an analog implementation and is thus chosen. It presents several advantages such as an easy implementation, versatility or fast response.

Runaway protection

When the current pass trough the Peltier element, the Peltier effect transfer heat from the cold to the hot side. But another effect comes into force too: the Joule effect. A special attention must be paid to the fact that the Joule effect can never overpass the Peltier effect. Otherwise, the temperature will rise, causing an increase of the current injected by the PID controller in the Peltier and increasing thus more this Joule effect. This endless loop phenomenon is called thermal runaway.

A system will be implemented in order to detect this non desired behaviour and switch off the Peltier current source. This implementation is not part of the framework of this thesis and will be designed in the near future.

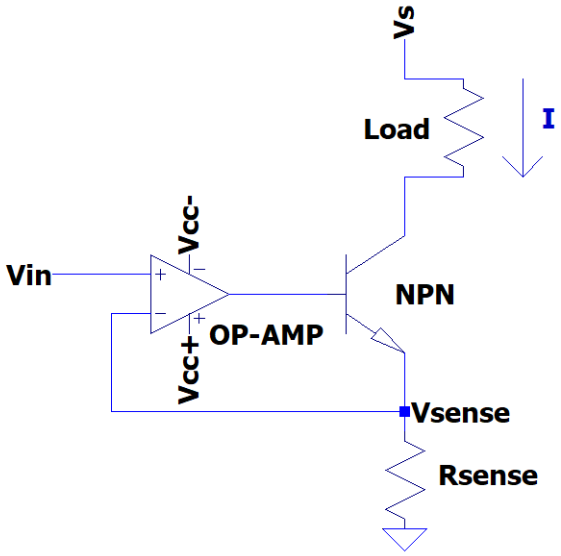

Figure 2.6 – Op-amp Current Source

2.3.2 Current source

The current passing trough the Peltier is provided by the op-amp/npn mounting shown in figure 2.6.

The main advantage of this setup is that the current is independent of the load. In theory, the op-amp will adjust its output in order to have equal voltages at its entries (+ & -). V_{in} is fixed by the PID controller upstream and fixed thus the value of V_{sense}. Thanks to the Ohm's law, an emitter current in the NPN transistor is created. The emitter current being equal to the collector current, the load is crossed by this current.

$$V_{in} = V_{sense} \tag{2.6}$$

$$I = \frac{V_{sense}}{R_{sense}} \tag{2.7}$$

$$I = \frac{V_{in}}{R_{sense}} \tag{2.8}$$

Limitations

Supply voltage The current drawn by the transistor is limited by the supply voltage V_s according to the load resistance (Ohm's law), the sensing resistor and the voltage drop across the transistor. R_{sense} must be thus carefully chosen in order to be big enough to convert the current into a stable sensing voltage V_{sense} but not too big to not overload the supply power voltage V_s.

NPN asymmetry The equation (2.7) implies the assumption that $I_c = I_e$ on the NPN transistor. But in fact, the collector current is equal to:

$$I_c = I_e - I_b = I_e - \frac{I_c}{\beta} \tag{2.9}$$

where β is the current gain.

So there is a difference between the current across sensing resistor and the current

across the load. In order to reduce as much as possible the error term, it is convenient to choose the transistor with a high beta. In fact, this current gain will vary between components, with the temperature and with aging. Furthermore, R_{sense} must be adapted according to that.

Choice of R_{sense} and V_s

The desired behaviour of the controller is: "For a maximum V_{in} value, having a maximum output current I". The V_{in} range is between 0V and 5V and the maximum current accepted by the Peltier is 0.4A. According to the equation (2.8), the R_{sense} value must be 12.5Ω.

The sensing voltage will be set at 5V when a maximum output response is needed. Thus, the 5V supply voltage can't be chosen because it will cause any voltage drop across the load. According to the Peltier data-sheet, the electrical resistance of the cooler is about 9Ω. So, the 12V supply voltage will be sufficient to give a constant current to the Peltier, proportional to V_{in}.

Due to the NPN asymmetry discussed above, collector and emitter currents are not equal. Regarding that β is not precisely known, adaptation will be done on the sensing resistor until reaching 0.4A in the Peltier element[1]. A value of 12.37Ω gives a 399,7mA (just below 0.4A) for a maximum value of V_{in} which is quite satisfying.

In practice, no resistor with such a precision can be found. This value will be rounded to 13Ω for example. The consequence of this is that an error will be added to the closed loop. Indeed, when a maximal response will be observed ($V_{in} = 5V$), the current will not be at its maximal value and thus a maximal temperature difference will not be observed between the TEC plates.

The impact on the dT term can be found thanks to the equation (2.1). The choice of this sensing resistor must be achieved with a practical implementation in order to really minimize this error.

2.3.3 Op-amp PID controller

A proportional–integral–derivative controller (PID) is a control loop mechanism which drives a system's output (here the detector's temperature) to a desired set point. Thanks to a feedback, an error is calculated and passed trough the 3 terms (proportional, integral and derivative) to bring the system to the desired output. The design of this controller is made in order to have a quick and accurate correction.

Three parameters (Kp, Ki and Kd) are the multipliers which are tuned in order to regulate the amount of each term in the final system configuration.

Error term

The first step of the process is to calculate the error term using the feedback and the set point value. This error is computed thanks to a differential op-amp schematized in figure 2.7.

Assuming that V_{set} is the set point which define the desired temperature and V_{temp} the voltage corresponding to the temperature measured in the detector. The relation between

[1]For simulation, a little resistor can be added in series to the Peltier to sense the current passing trough it. Indeed, the current source is load independent (for small load changes).

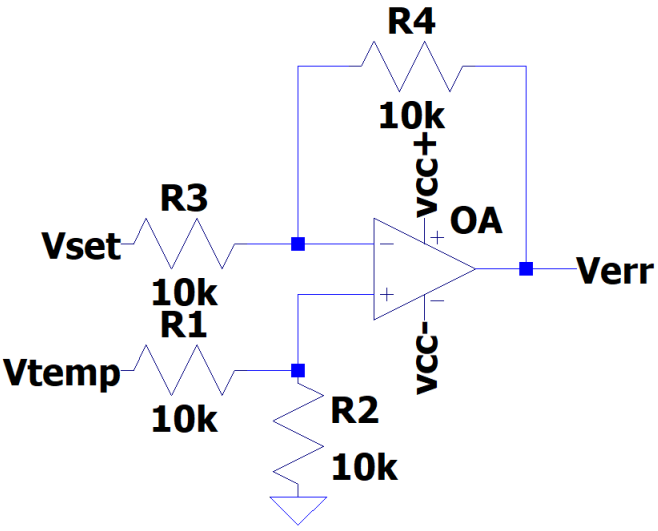

Figure 2.7 – Error amplifier

temperature and voltage is defined by:

$$\begin{cases} V(0°C) = 636mV \\ slope = -2.183mV/°C \end{cases} \tag{2.10}$$

$$\Rightarrow V[V] = 636 * 10^{-3} - (T[°C] * 2.183 * 10^{-3}) \tag{2.11}$$

The output of the differential mounting is proportional to the difference of the 2 inputs:

$$V_{err} = V_{temp}\left(\frac{(R_4 + R_3)\,R_2}{(R_2 + R_1)\,R_3}\right) - V_{set}\left(\frac{R_4}{R_3}\right) \tag{2.12}$$

Thus, if $R_1 = R_2 = R_3 = R_4$:

$$V_{err} = V_{temp} - V_{set} = -error \tag{2.13}$$

which is the inverted error.

Proportional term

The proportional term is the main drive in the controller because it reduces a large part of the overall error. This term is achieved by an inverting amplifier like illustrated in figure 2.8.

The gain of this configuration is given by the ratio of the two resistors:

$$V_p = -V_{err} * \frac{R6}{R5} \tag{2.14}$$

So, if the values of resistors in figure 2.8 are kept, the proportional term is:

$$P = V_p = -V_{err} * \frac{K_p * 1k}{1k} = error * K_p \tag{2.15}$$

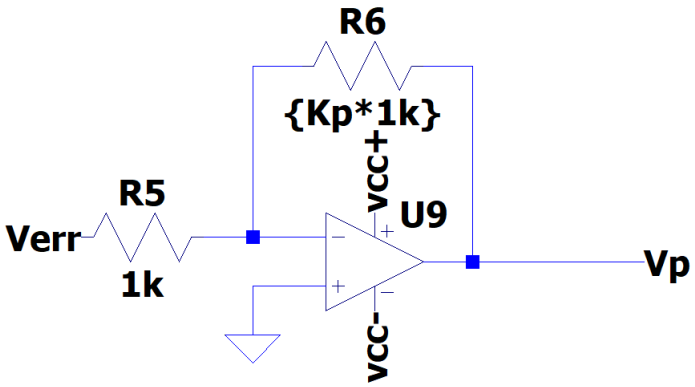

Figure 2.8 – Proportional term

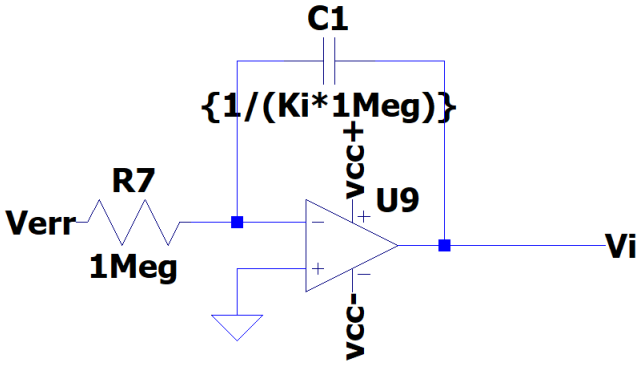

Figure 2.9 – Integral term

Small gain leads to a small response (maybe too small to respond to a disturbance) and too high gain lead to unstable response (oscillations).

Integral term

The integral term will correct the accumulated error in the controller. It sums the actual error over time. This term is achieved by an integrator op-amp like illustrated in figure 2.9.

The current passing trough R_7 is integrated trough C_1:

$$i(t) = \frac{V_{err}(t)}{R7} \tag{2.16}$$

$$V_i(t) = -\frac{1}{C_1}\int_0^t i(t)dt \tag{2.17}$$

So, if the values of R_7 and C_1 in figure 2.9 are kept, the integral term is:

$$I = V_i(t) = -K_i \int_0^t V_{err}(t)dt = K_i \int_0^t error(t) \tag{2.18}$$

This principle will accelerate the response and eliminate steady-state error from the

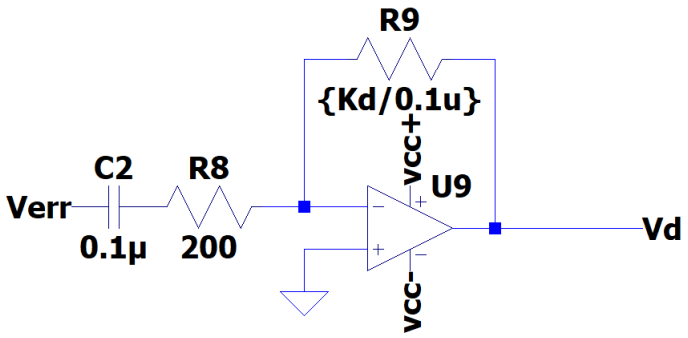

Figure 2.10 – Derivative term

P-term. On the other hand, this term will also produce overshoot if it is too important.

Derivative term

In order to counteract the P- and I-terms when the response change quickly, the derivative term will smooth the response by reducing overshooting and ringing. This term is achieved by a differentiator op-amp like illustrated in figure 2.10.

The input voltage variations across C_2 will produce a current trough the resistor R_9:

$$i(t) = C_2 * \frac{dV_{err}}{dt} V_d(t) = -i(t) * R_9 = -C_2 * R_9 * \frac{dV_{err}}{dt} \tag{2.19}$$

So, if the values of R_9 and C_2 in figure 2.10 are kept, the derivative term is:

$$D = V_d(t) = -K_d * \frac{dV_{err}}{dt} = K_d * \frac{derror}{dt} \tag{2.20}$$

This circuit is a high-pass filter too, so it may amplify unwanted disturbances or noises. The resistance R_8 is here to avoid that by limiting the high frequency gain at $G = \frac{R_9}{R_8}$. Furthermore, this resistor reduces phase-shift added by the 2 other passive elements, especially at high frequencies.

Summing and inverting stages

These two stages are illustrated in figure 2.11.

First, the summing op-amp regroups the three terms into one inverted output. The ratio of each term can be adjusted thanks to the resistors in each term branch. In figure 2.11, the ratios are all the same. With these resistors can also be added mechanical switches in the case of willing deactivate one of the three terms.

Because the output is once again inverted, a second stage is needed to reverse the signal. Furthermore, this inverting amplifier is powered up with a positive supply only. Indeed, the Peltier element can only cool, not heat. So there is no need for a negative current passing through it. The signal is also amplified in order to have a good behaviour: close to saturation when the error is the maximum admitted.

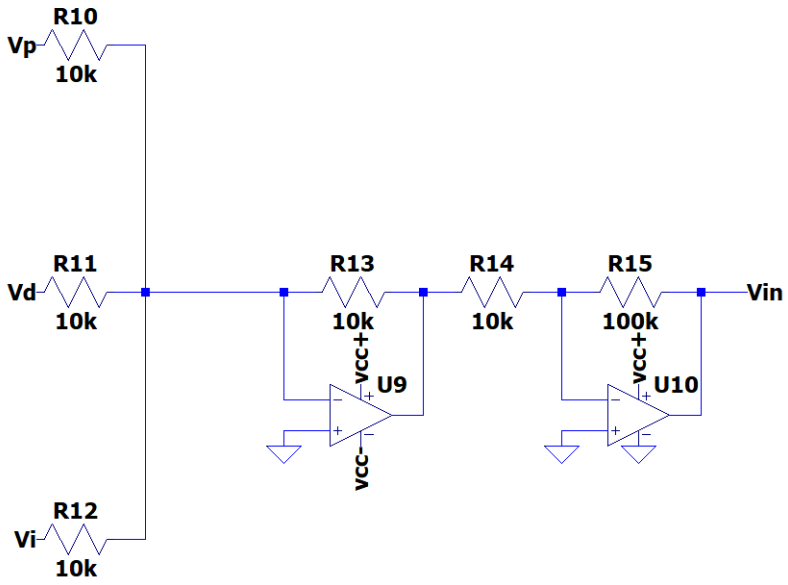

Figure 2.11 – Summing and inverting stages

2.3.4 Set-point voltage

Design

In order to generate the set-point which be of the order of a few hundreds of millivolts, a reference voltage will be used. RH1009 component is a general purpose 2.5V shunt regulator diode designed to operate over a wide current range while maintaining good stability with time and temperature. The 5V supply can be connected to it through a protection resistor in order to be under the maximum forward current (10mA). So, this resistor must have a value under 500 ohms. With this, a stable 2.5V point is obtained.

The second part is a voltage divider to achieve the desired set-point. The total circuit is shown in figure 2.12.

The relation between the set-point voltage and the resistors ratio is:

$$\frac{V_{set}}{2.5} = \frac{R_2}{R_1 + R_2} \tag{2.21}$$

$$\Leftrightarrow \frac{R_1}{R_2} = \frac{2.5}{V_{set}} - 1 \tag{2.22}$$

Choice of the value

The goal of the controller will be to maintain a stable temperature of the detector as low as possible under any perturbation.

From the detector packaging description, it can be assumes that the ambient temperature of the electronics is the temperature in contact with the hot plate of the Peltier (via a radiator). If the future thermal design is assumed to be coherent with the data-sheet specifications, this temperature will not exceed 30°C (in the worst case).

Always according to the SDD data-sheet, under a maximal heat flux of 0.35W (worst perturbation), the maximal temperature gradient produced by the Peltier cooler will be 20K (with max current, 0.4A). This behaviour can be seen in figure 2.2.

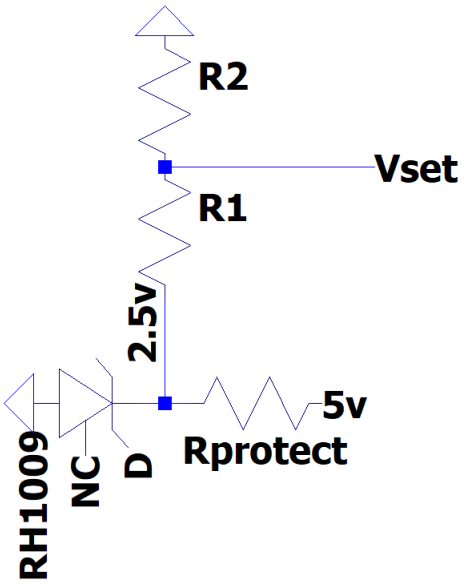

Figure 2.12 – Set-point voltage

Bringing these two information together, the lower possible set-point can be set at 10°C in order to maintain a stable behaviour in the worst case (max. ambient temp. and max. heat flux). This corresponds to a voltage of 614.17mV. According to equation (2.22), the resistors ratio R_1/R_2 is equal to 3.07.

2.3.5 PID tuning

The tuning of the parameter will be realised manually by trial and error. The parameter are incremented in a methodical way and the step response of the PID is evaluated for each change. The step response is the response of the temperature curve from the detector in response to a step of the disruptive parameter: the input heat flux. This step is maximal and instantaneous: +0.35W in 1µs.

Here is the method to tune parameters:

1. Connect proportional term with $K_p = 1$ ($R = 1k\Omega$).
2. Increase K_p until obtain oscillations or overshoot.
3. Take the last stable value of K_p and connect integral term with $K_i = 1$ ($C = 1\mu F$).
4. Increase K_i until obtain satisfying response or oscillations (overshoot).
5. If the response need to be smooth, connect derivative term with $K_d = 0.1\mu$.
6. Increase K_d until obtain satisfying response.

2.3.6 Current source for temperature pin

The temperature diode requires a bias current of 45µA. To achieve this, a current source similar to the one implemented for the Peltier cooler (Subsection 2.3.2) is created. One modification is done: according to the fact that the output voltage is connected to a

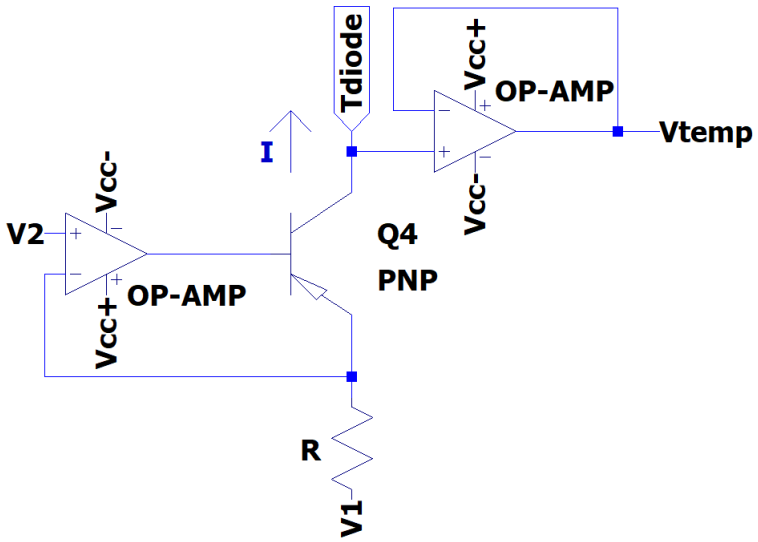

Figure 2.13 – Current source for diode bias

voltage divider, a leakage current will appear and an additional buffer stage is added. The setup is illustrated in figure 2.13.

In this configuration, the voltage V_2 is transferred to the emitter of the transistor. So the current passing through the transistor is equal to:

$$I = \frac{V_1 - V_2}{R} \tag{2.23}$$

and is independent of the load (from the diode).

The PNP asymmetry limitation is the same as discussed previously for NPN and a practical implementation with a high-β transistor needs to be made in order to adjust R to have the precise value for the current.

If the 2 low voltages for V_1 and V_2 are 12V & 5V, a theoretical value for R will be:

$$R = \frac{12 - 5}{45\mu} = 155555,556$$

This value cannot be precisely obtained, but can be approached by a series of resistors with standard values.

2.4 Simulations

The simulations were performed using LTSpice XVII.

The model simulating the op-amps is UniversalOpAmp2 (included in LTSpice) which is a single pole op-amp with one internal node, slew rate limit and output voltage and current limit. The limit values are adjustable so that model is versatile for simulating real op-amps (according to their data-sheets).

The resistors are assumed to be ideal (no tolerance or power rating) and the capacitors too (no voltage/current rating, no equivalent series/parallel resistance, capacitance or inductance). Bipolar transistors are simulated with their basic model too.

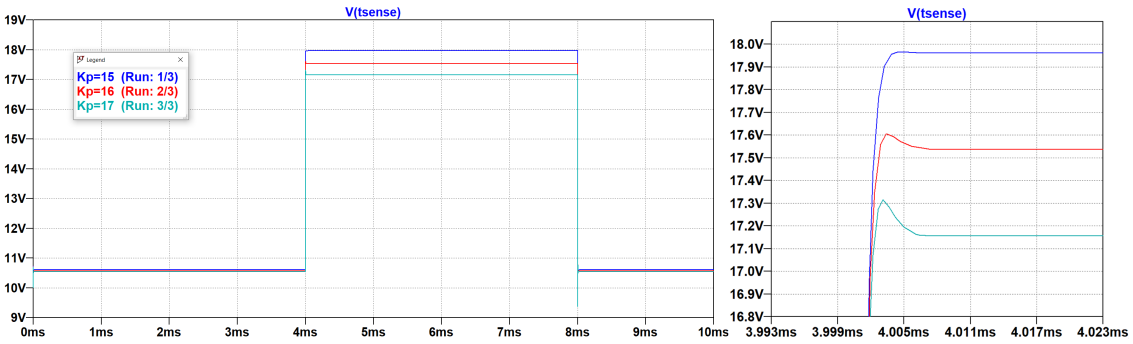

Figure 2.14 – Temperature response with different values for K_p

2.4.1 PID tuning

In this subsection, the method to tune K_p, K_i and K_d described previously is applied to the system. The perturbation is an instantaneous increase of heat flux from 0W to 0.35W at 4ms. This value comes back to 0W at 8ms.

The first step is to connect only the proportional term and to increase K_p until oscillations or overshoot on the response appear. The incrementation has been made with respect to the standard resistor values since $R = K_p \times 1k$.

As can be seen in figure 2.14, an overshoot appears from $K_p = 16$. Another phenomenon is observed here: the steady-state error. This error remains even with no incoming heat flux. When $Q_{in} = 0$, this error is less than 1°C and when $Q_{in} = 0.35W$ this error is 7.96°C. Indeed, if the proportional term is increased, this steady-state error decreases but overshoot increases too. There is thus a first trade-off. Anyway, the value $K_p = 15$ is thus kept to avoid overshoot.

The steady-state error problem will be treated with the second step: connecting the integral term. Increasing the K_i term is equivalent to reduce the capacitor value. After several tests, the temperature seems not to present overshoot or oscillations even with very large value for K_i.

As previously explained, this term accelerates the response. This can be seen in figure 2.15. The largest possible value is 100k which corresponds to a 10 pF capacitor. Capacitor with smaller value are existing but 10 pF is already a sufficient choice. The steady state error is eliminated in less than 1 ms, which is quite satisfying.

The peak is not an overshoot, but is produced by the abrupt change of state in the Peltier element. This peak is about 7.36°C over the target, but is quickly compensated.

Finally, the derivative term is connected to flatten the peak and smooth the curve. The increment is made with respect to the standard resistor values since $R = K_d/0.1\mu$. This increase was stopped at $K_d = 680\mu$ because high-frequency oscillations was observed beyond this value.

As can be seen in figure 2.16, the influence of the derivative term is to reduce the height of the peak (5°C for $K_d = 680\mu$) and smooth the sharp shape of the curve. On the other hand, the response time is increased too. The cold side of the Peltier joins the set-point temperature after a bit more than 1ms.

A zoom on the upper side of the peak permit to see a little oscillation, more present with greater K_d values. Once again, a tradeoff is posed between peak reduction versus response time and this upper oscillation appearance. The value of $K_d = 680\mu$ is finally kept.

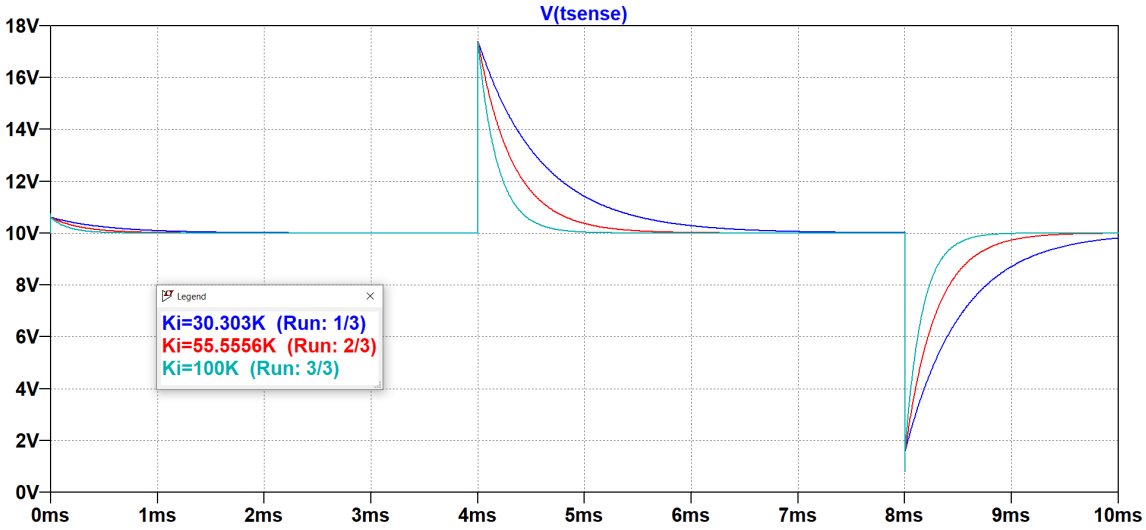

Figure 2.15 – Temperature response with different values for K_i and with $K_p = 15$

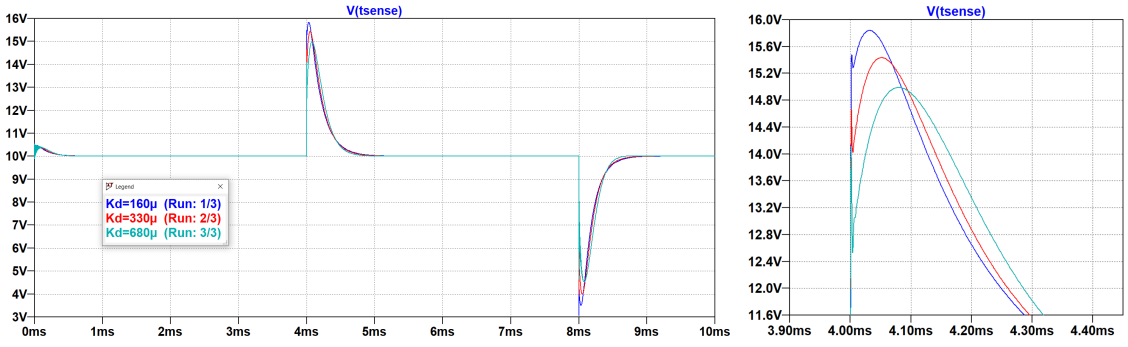

Figure 2.16 – Temperature response with different values for K_d, with $K_p = 15$ and $K_i = 100k$

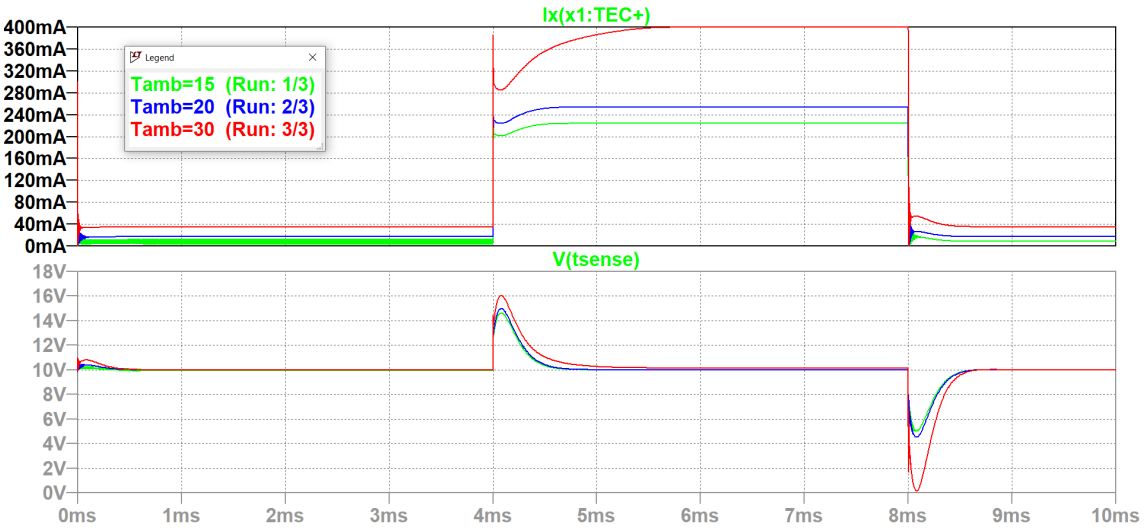

Figure 2.17 – Current and temperature response with different values for ambient temp.

2.4.2 Influence of ambient temperature

In figure 2.17, the behaviour of the Peltier driving current can be observed. Several ambient temperatures were tested in the range of optimal operation (10°C to 30°C). This ambient temperature is assumed to be always greater than the cold side of the Peltier. When this ambient temperature is 30°C, a saturation of the Peltier current is produced by the controller (400mA) when the incoming heat flux is maximal.This is the expected behaviour and the tiny steady-state error is due to the thermal resistance of the radiator (0.2 ohm resistor in simulation). As expected too, further the ambient temperature is from the set-point, slower and bigger the response in temperature is.

2.5 Conclusion

In this chapter, a current source controlled by an analog PID controller has been implemented in order to supply a Peltier cooler. The purpose of the controller is to stabilize the temperature of the X-rays detector chip. The controller reacts well to a step function with maximum input heat flux. Indeed, the temperature is stabilized in approximately 1ms in a smooth way (5°C peak in worst case).

The first challenge was to design a simulation model for the Peltier element. This task was achieved using the TEC data-sheet. The temperature difference curves simulated are very close to the real ones (from the data-sheet). Then an analog current source was implemented in order to have constant current (drive by an input voltage) regardless of the load with a maximum current value. This input voltage was controlled by an analog PID controller. This circuit was mainly composed of 3 stages: a proportional term, an integral term and a derivative term. A reasonable set-point (temperature) was defined and the error between this set-point and the measured temperature was passed through this 3 stages.

Finally, the parameters of the controller have been tuned trough simulations on LTSpice XVII. The method for tuning these parameters can be reused for practical implementation. The response in current have the expected behaviour: fast, stable and smooth. The temperature is stabilised on the targeted value in a satisfying way.

Practical implementation

This study is the basis of a practical implementation. The PID parameters must be adapted to the real Peltier behaviour.

Firstly, the sensing resistor of the current sources (for the Peltier and the diode bias) must be adapted in order to obtain precisely the required current in the target. The bipolar transistors must be chosen with a high β factor to reduce the error.

Secondly, the method described in the subsection 2.3.5 can be reused to adjust real parameters. This manual method is based on trial and error. Other more sophisticated methods exists, but require higher skills in linear control systems (which are out of the scope of this thesis) or deep analysis of the Peltier element response and the feedback loop. For this project, the manual method will be sufficient.

Thirdly, as discussed in subsection 2.3.1, a runaway protection mechanism is necessary for the safety of the electronics and detector chip. This feature will be implemented in a near future.

Fourthly, the set-point of temperature, actually on 10°C can be changed to a lower value in order to have better detector performances. But this change must be made conscientiously knowing the environmental conditions and the fact that the Peltier can not produce dT over 20K under a maximum incoming heat flux of 0.35W (the whole Peltier behaviour has to be taken into account too).

Finally, the utility of the derivative part can be more discussed. In order to offer the possibility to evaluate each term, mechanical switches will be present on the test board. If a term is useless (more likely the derivative term), it will be removed on the final PCB to gain in term of place, power consumption and cost.

Chapter 3
Switchable voltage source for the X-ray generators

This third chapter will study the design of a self-switching voltage source in order to power the X-ray generators. First of all, the goal and specifications of the controller and the sources will be clearly explained. Next, the actual circuit from Amptek will be practically observed in order to get more information. Then, the design of a Schmitt trigger will be chosen to fulfill the asked task. Given the fact that the output voltage has to be alterable, the next section will implement a variable gain attenuator. Finally, simulations will be performed on LTSpice and a conclusion will describe the next steps for practical implementation.

3.1 Purpose and specifications

When a pyroelectric crystal is heated, a spontaneous decrease of polarization is observed and an electric field develops across the crystal. Thanks to its specific orientation, the top surface which becomes positively charged attracts electrons from the low pressure gas in the environment. These electrons accumulate on the surface and produce Ta characteristic X-rays (and bremsstrahlung X-rays).

When the cooling phase starts, a spontaneous increase of polarization is observed and the electrons from the top surface of the crystal are accelerated toward the Cu target (at ground potential). Cu characteristic X-rays are thus produced (as well as bremsstrahlung X-rays).

This principle is illustrated in figure 3.1.

The purpose of the controller is to supply power to the X-ray generator and automatically change the heating and cooling phases of the cycle.

3.1.1 Data-sheet specifications

The X-ray generator includes 3 pins. First, a temperature pin which must be connected to a 1mA current source in order to read out the temperature voltage. Second, a heater voltage input which is the output of the controller. The ”on” state is driven by a voltage between 2.5V and 4.5V DC and the ”off” state is driven by a zero voltage. The last pin is a ground connection.

The cycle time of the COOL-X can be varied from 2 to 5 minutes. The heater is driven by one low and one high temperature trigger points.

3.2 Measurements on the actual controller

Unfortunately, the data-sheet specifies neither the voltage-temperature curve nor the high and low temperature points. Reverse engineering has to be made in order to find these points (the voltage-temperature curve is not specially very important for the control part except for the slope sign).

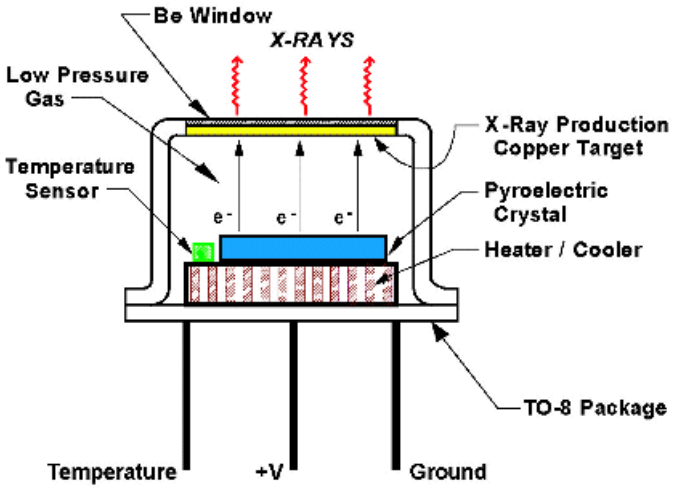

Figure 3.1 – Cool-X layout [2]

3.2.1 Observation of the circuit

Just by opening the metal box and by observing the circuit from the top side, the fact that 3 values can be adjusted is confirmed: the high and low temperature points and the heater power. These variables are alterable with 3 potentiometers. The goal here is not to change them, but to reproduce the same behaviour.

A 3-terminal is also present with 3 wires starting from it and going to the emitter itself: a black one for the ground, a red one for the heater voltage and a yellow one for the temperature readout.

The resistance of the heater is measured at ambient temperature. It presents a value of 13 ohms. Naturally, this value will vary with the temperature, but gives the magnitude of the load.

When working, a flashing led indicate if the generator is in its cooling (green) or heating phase (red) and a beep sound is heard when the transition is made.

3.2.2 Oscilloscope observation

The heater voltage and the temperature feedback voltage were observed on a Tektronix MSO2024B oscilloscope while the generator was working. An integrated 1Hz-Noise filter was applied in order to have smooth signals. These traces are shown in figure 3.2.

The first observation is that the temperature voltage is inversely proportional to the temperature. Next, V_{on} is at 344mV, the high temperature voltage is at 42.8mV and the low temperature voltage at 58.8mV. In this configuration, one cycle (heat phase + cold phase) lasts 114.91 seconds ($\sim$ 2 minutes).

The measurement setup is shown in figure 3.3. Radiation precautions were made. The X-rays source was furnished with a thick cap in order to attenuate the dangerous emissions. A test with a Geiger counter was performed in order to prove the efficiency of this cap. The emitted X-rays are low energy, so that the absorption of the cap is sufficient thanks to its thickness. The Geiger counter does not activate with the cap. Indeed, radiation does not pass or their number are under the natural background noise.

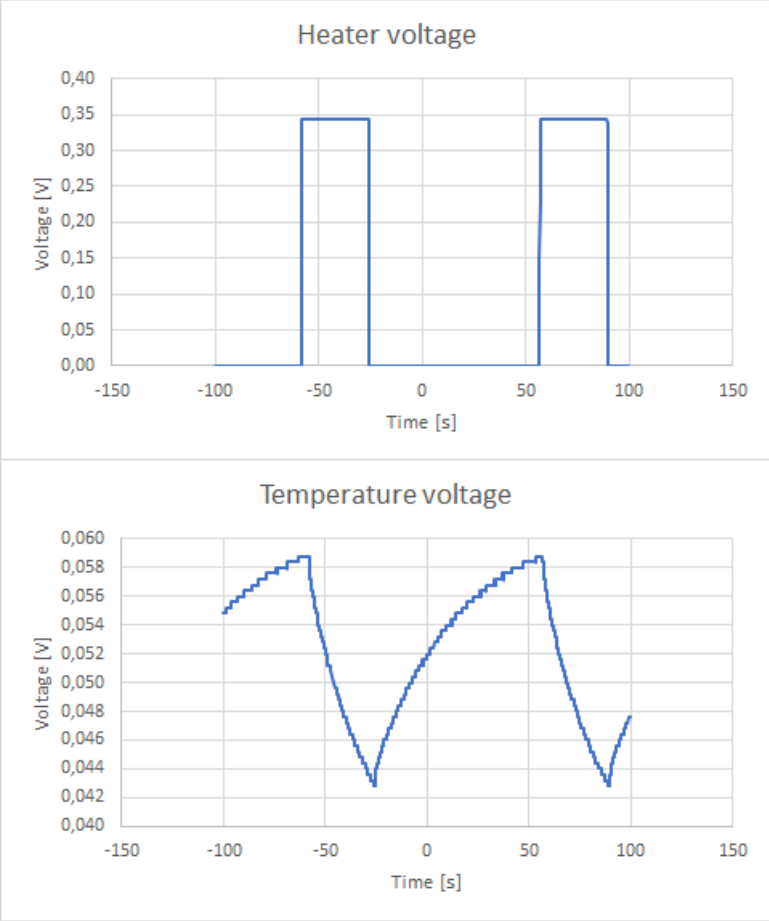

Figure 3.2 – Heater and temperature voltages

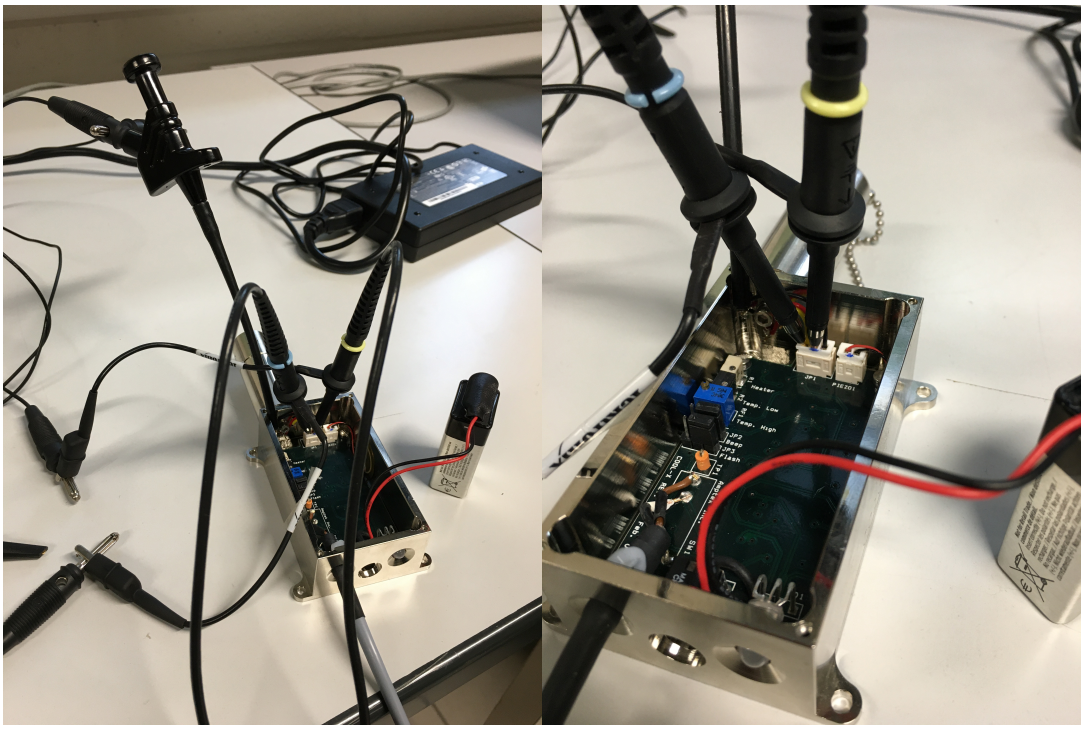

Figure 3.3 – Lab setup to measure heater (yellow clamp) and temperature (blue clamp) voltages

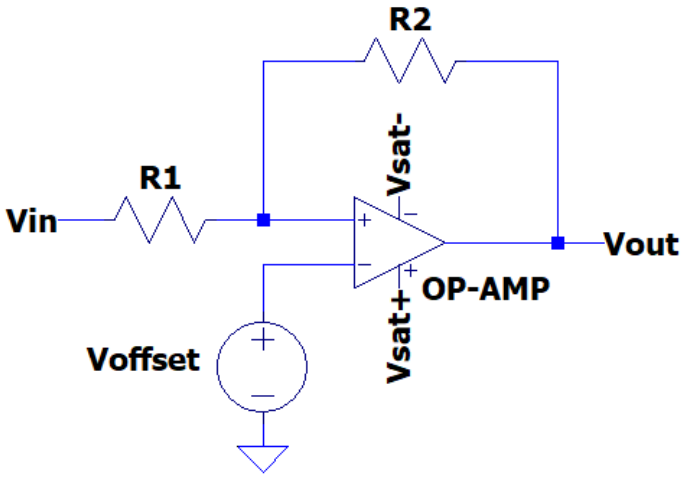

Figure 3.4 – Non inverting Schmitt trigger using op-amp

3.2.3 Discussion about controller topology

According to the inverse relationship between temperature and voltage, the controller must switch the voltage on when the temperature voltage goes over a high point and switch off this voltage when the temperature voltage goes below a low point. This feature can be exploited by a non inverting Schmitt trigger.

The first issue is the too little voltage difference between high and low temperature point (16mV). To deal with that, an amplifying stage will be added upstream the Schmitt trigger.

The second problem is that the Schmitt trigger mounting is highly dependent of all its parameters, including its supply voltage. In order to get rid of this supply voltage dependence, a Zener diode can be add between ground and output to fix the ”on” output voltage to its breakdown voltage. A resistor must be added too to limit the current passing trough the diode.

Finally, the difference between data-sheet information and reality measurement of the heater voltage ($\sim$ 10 factor) bring a new reflection: the power sent to the heater must be programmable in order to anticipate unknown behaviour in space. Practically, an attenuating (or amplifying regarding the Zener voltage) stage will be added next to the Schmitt trigger and this stage will include a variable gain which can be controlled digitally.

3.3 Non inverting Schmitt trigger comparator

3.3.1 Principle of operation

The circuit is illustrated in figure 3.4. As it can be seen, there is a positive feedback causing a saturating behaviour of the op-amp. V_{out} can thus only be equal to V_{sat+} or V_{sat-}.

The input voltages are:

$$V_- = V_{offset} \tag{3.1}$$

$$V_+ = \frac{V_{in}R_2 + V_{out}R_1}{R_1 + R_2} \tag{3.2}$$

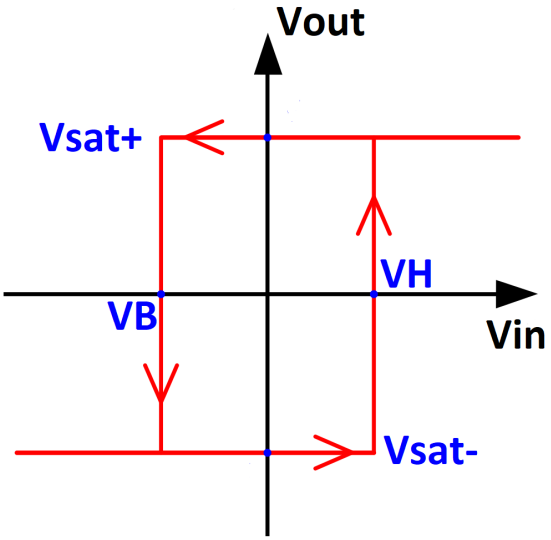

Figure 3.5 – Transfer function of a non inverting Schmitt trigger

If $V_{out} = V_{sat-}$, the trigger to V_{sat+} is operated when $V_+ > V_{offset}$:

$$\Leftrightarrow \frac{V_{in}R_2 + V_{out}R_1}{R_1 + R_2} > V_{offset} \tag{3.3}$$

$$\Leftrightarrow V_{in}R_2 + V_{out}R_1 > V_{offset}(R_1 + R_2) \tag{3.4}$$

$$\Leftrightarrow V_{in} > V_{offset}(1 + \frac{R_1}{R_2}) - V_{out}\frac{R_1}{R_2} \tag{3.5}$$

$$\Leftrightarrow V_{in} > V_{offset}(1 + \frac{R_1}{R_2}) - V_{sat-}\frac{R_1}{R_2} = V_H \tag{3.6}$$

If $V_{out} = V_{sat+}$, the trigger to V_{sat-} is operated when $V_+ < V_{offset}$:

$$\Leftrightarrow V_{in} < V_{offset}(1 + \frac{R_1}{R_2}) - V_{out}\frac{R_1}{R_2} \tag{3.7}$$

$$\Leftrightarrow V_{in} < V_{offset}(1 + \frac{R_1}{R_2}) - V_{sat+}\frac{R_1}{R_2} = V_B \tag{3.8}$$

The transfer function is illustrated in figure 3.5.

3.3.2 Adding a Zener diode

Choice of the diode

The breakdown voltage must be close, but smaller than the ”on” output voltage of the op-amp (V_{sat+}). Knowing that diodes with small breakdown voltage present bad I-V characteristic curves, the choice of an +12V/GND supply voltages is made. Thanks to that, a 10V Zener voltage is chosen which is acceptable because of the fact that real op-amp saturation voltage is smaller than the supply voltage.

A protection resistor must also be added in series between the op-amp output and the Zener in order to limit the current flowing trough it. Because the potential difference which will cross it will be not above 2V, a 700Ω resistor will limit the current less than 3mA.

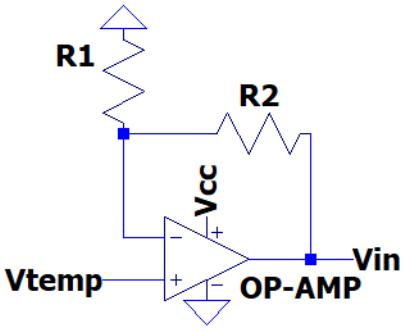

Figure 3.6 – Pre-amplifying stage for the Schmitt trigger

Adaptation to the problem

V_{sat-} will be the off voltage and so will be equal to the built-in potential of the diode (0.7V). V_{sat+} is the on voltage, equal to the Zener breakdown voltage, 10V. V_H and V_B are respectively the low and high temperature point corresponding voltages.

If the offset voltage is fixed by a voltage reference, here RH1009 is chosen (2.5V), the equations (3.8) and (3.6) become:

$$V_B = 2.5(1 + \frac{R_1}{R_2}) - 10\frac{R_1}{R_2} \tag{3.9}$$

$$V_H = 2.5(1 + \frac{R_1}{R_2}) - 0.7\frac{R_1}{R_2} \tag{3.10}$$

3.3.3 Adding an amplifier stage

In order to have a sufficient difference between high and low point, a simple non-inverting amplifying stage is the first step of the mounting. The schematic of this amplifier is shown in figure 3.6.

The resistor values are chosen in order to fit with the desired gain. Indeed, the equation of the ideal amplifier is:

$$G = \frac{V_{out}}{V_{in}} = (1 + \frac{R_1}{R_2}) \tag{3.11}$$

But due to the finite amplifying term A, it becomes:

$$G = \frac{(R_1 + R_2)A}{(1 + A)R_1 + R_2} \tag{3.12}$$

And this term is not known.

Equations

This stage adds new equations to the system:

$$V_B = V_b * G \tag{3.13}$$

$$V_H = V_h * G \tag{3.14}$$

where V_h and V_b are the initial low and high voltage points (not amplified).

3.3.4 Choice of the amplifier gain and Schmitt resistor values

Knowing the high and low voltage points, not amplified (42.8mV and 58.8mV), 2 equations with 2 unknowns are found from equations (3.9), (3.10), (3.13) and (3.14):

$$\begin{cases} 0.0428 * G = 2.5(1 + \frac{R_1}{R_2}) - 10\frac{R_1}{R_2} \\ 0.0588 * G = 2.5(1 + \frac{R_1}{R_2}) - 0.7\frac{R_1}{R_2} \end{cases} \tag{3.15}$$

The resolution of this system gives:

$$\begin{cases} \frac{R_1}{R_2} = \frac{1000}{12951} \\ G = 44.8807 \end{cases} \tag{3.16}$$

3.3.5 Current source for temperature sensor

The temperature sensor needs a current source of 1mA to work correctly. The design of this current source is implemented on the same basis than in Chapter 2 subsection 2.3.6.

Two modifications have to be made in order to ensure correct working. First, the value of the resistor changes because the current is not the same. According to equation (2.23), R is equal to $7k\Omega$.

Secondly, according to the fact that the output voltage is connected directly to an operational amplifier (high impedance), the buffer is useless and is removed. The circuit is thus the same (without the second amplifier) than in the figure 2.13.

3.4 Variable gain attenuator

The 10V/∼0V signal must be attenuated in order to respect data-sheet specification.

A resistor divider followed by a buffer will do this task. The second resistor of the potential divider will be replaced by a digital potentiometer to add the digitally controlled gain side.

But using an op-amp output directly to the load is a problem: the output power is limited by the maximum output current flowing from the op-amp and by the load:

$$P_{max} = R_{load} \times I^2_{out,max} \tag{3.17}$$

To overcome this problem, an NPN transistor is added on the op-amp output. The negative feedback branch is displaced on the emitter of the transistor and connected to the load. A supply voltage is added on the collector side to power up this setup. The circuit is schematised in figure 3.7.

The negative input voltage (output of the potential divider) is simply repeated at the NPN emitter (in the limit of the supply voltage) and can be expressed by the following equation:

$$V_{out} = V_- = \frac{R_{pot}}{R_1 + R_{pot}} V_{trig} \tag{3.18}$$

R_1 is fixed at $30k\Omega$ and V_{trig} can take the values 10V or ∼ 0V.

Choice of V_s and limitations

The supply voltage must be chosen large enough to support all the voltages the voltage divider will produces. Also, a particular attention must be made on the supply voltage for

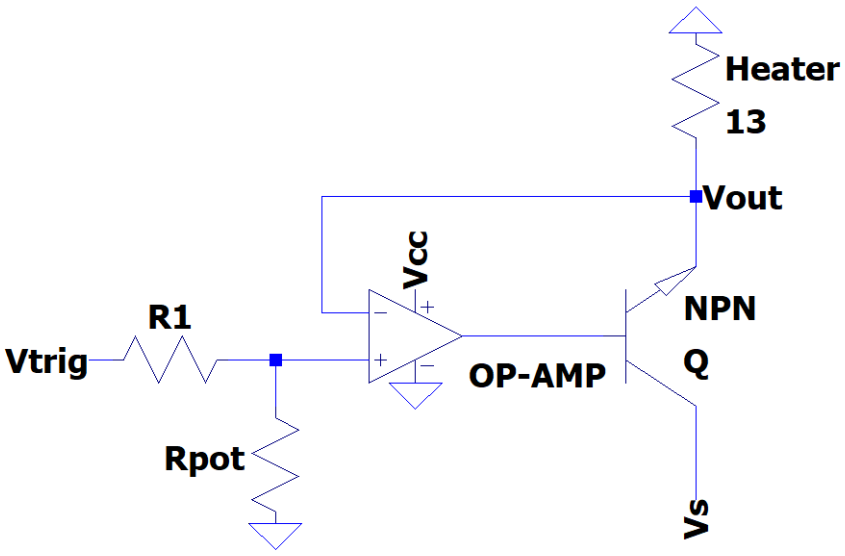

Figure 3.7 – Voltage divider followed by a buffer op-amp

the op-amp. Indeed, its output must not saturate (linear behaviour) in order to correctly reproduce the positive input on the negative feedback. For this design $V_s = 5V$ is sufficient with a 0/+12V supply for the op-amp.

3.4.1 Digital potentiometer implementation

Thanks to an analog demultiplexer coupled with a series of resistors, a digital potentiometer can be implemented. As a function of the 3-bit of logic inputs, the total value of the resistor is changed so that the attenuator's gain.

The multiplexer is chosen according 3 criteria: the size, the qualification and its configuration. Most of the multiplexer in the ESCC list is presented in FP-16 (Flat Package-16 pins). The 4051B type is suitable for this application because it is a single 8-channel multiplexer/demultiplexer. This gives the advantage to obtain a range of 8 voltages with 3 digital bits. Model HCF4051 from ST has a low "on" resistance of 125 ohms for a 15V supply voltage (180 ohms for 10V).

The resistors are chosen with the usual values in order to have at the output approximately the following values: minimum and maximum "on" voltages specified by the data-sheet (2.5V & 4.5V), the middle of these 2 values (3.5V), these 3 values decreased by the 10 factor in order to obtain the magnitude of the measurements (250, 350 & 450 mV) and 2 additional values between these 2 groups of voltages (1.2V & 1.9V). The first resistor value is chosen according to the "on" resistance of the multiplexer.

The resistors are all placed in series with a channel of the multiplexer connected to each junction. The common channel is at ground. This configuration allows the user to choose where the ground is placed on the resistors series and thus choose the total resistance value. The setup is shown in figure 3.8 and the truth table of the multiplexer, coupled with the corresponding resistances and "on" output voltages is described on table 3.1.

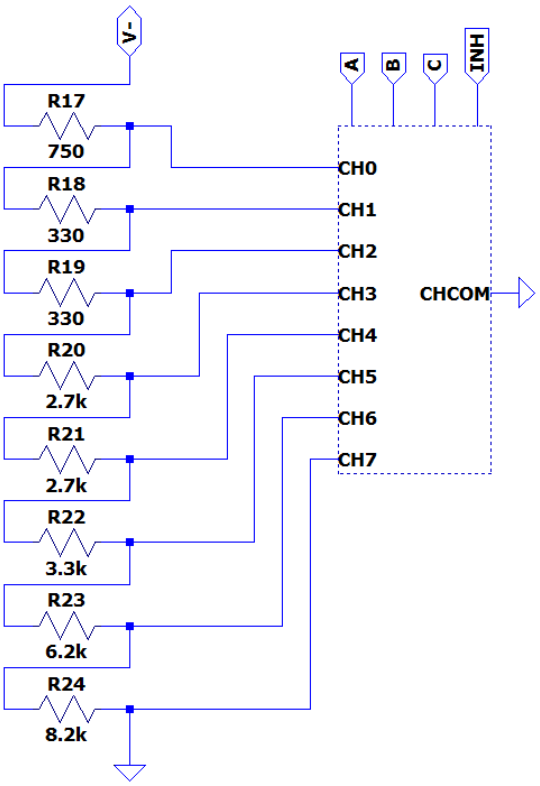

Figure 3.8 – Digital potentiometer

Control inputs				"On" channel	R_{pot} [Ohms]	"On" divided voltage [Volts]
INH	Select					
	C	B	A			
0	0	0	0	0	750	0.244
0	0	0	1	1	1080	0.348
0	0	1	0	2	1410	0.449
0	0	1	1	3	4.11k	1.208
0	1	0	0	4	6.81k	1.855
0	1	0	1	5	10.11k	2.527
0	1	1	0	6	16.31k	3.532
0	1	1	1	7	24.51k	4.357
1	x	x	x	None	24.51k	4.357

Table 3.1 – Truth table of the digital potentiometer

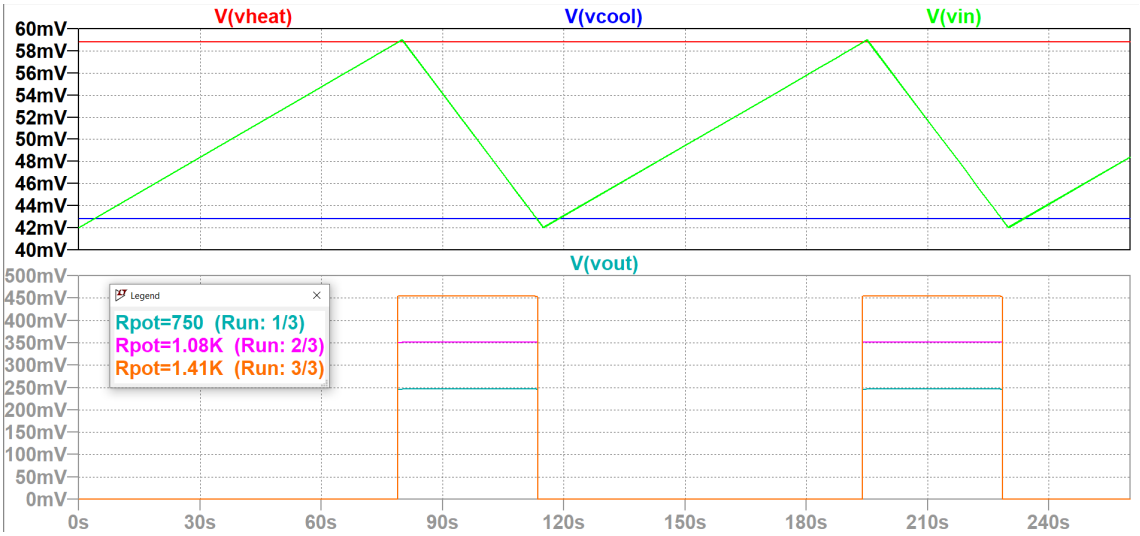

Figure 3.9 – Simulation of the source controller

3.5 Simulations

The simulations were performed using LTSpice XVII.

The model simulating the op-amps is UniversalOpAmp2 (included in LTSpice) which is a single pole op-amp with one internal node, slew rate limit and output voltage and current limit. The limit values are adjustable so that model is versatile for simulating real op-amps (according to their data-sheets).

The resistors are assumed to be ideal (no tolerance or power rating). The Zener diode is chosen in the library with the same breakdown voltage than in the design (10V) and the RH1009 has its own model in LTSpice. Bipolar transistors are simulated with their basic model too.

In order to have a simulation coherent with real measurements, the rise and fall times of the temperature voltage are the same than measured in section 3.2. Even if the rise is linear, the shape of the curve is not a big deal for this type of controller.

The digital potentiometer can not be implemented in an analogical simulation program so it is replaced by a simple resistor. Given the fact that the configuration around the 3.5V output has few unknowns (specially the load impedance), simulations will be only for output values around the actual setup (350mV output, 13 ohm load). These simulations are shown in figure 3.9. As can be seen, the controller plays its role perfectly. When the input voltage (from the temperature sensor) overstep 58.8mV (value when the heater must be turned ”on”), the output voltage rises to the desired value (250, 350 or 450mV according to the digital potentiometer value). When the voltage goes under 42.8mV (value when the heater must be turned ”off), the output voltage jumps to 0V and the source will cool down.

Even if the input voltage crosses one voltage limit 2 times in a row, the heater will not change its state. That is exactly the expected behaviour of a Schmitt trigger with 2 thresholds.

3.6 Conclusion

The analog controller implemented here works perfectly in the same way than the actual commercial one. This circuit will be repeated two times in order to supply two sources independently (6 times in the final version).

Starting from the Cool-X generator data-sheet from Amptek, the study has begun with real test measurement in order to see the actual working conditions. An analog design has been implemented from scratch in order to fill these requirements. A non inverting Schmitt trigger comparator is the heart of this design because it produces a hysteresis behavior which is suitable for this self-switching voltage source. Other features have been implemented such as a digital potentiometer to modify the output voltage, an input amplifier stage to have sufficient difference between high and low points and an analog current source for biasing the temperature sensor.

The conclusion of this chapter is a simulation with the conditions from the actual configuration. This simulation gives satisfying results. Indeed, the behaviour of the output voltage is the same than in the actual controller (from Amptek). The temperature thresholds are correctly detected and the heater switch from ”on” state to ”off” correctly.

Practical implementation

The next step following this work is a real implementation of the controller in order to fix some details and see the real behaviour of this Schmitt trigger with non ideal components.

First, the gain given by the system (3.16) is fixed by the 2 resistors from the pre-amplifying stage. The value of these resistors has to be chosen according to the amplifier behaviour in order to have an output 44.88 times greater than the input.

Second, the current source resistor has to be adjusted to get precisely a 1mA current on the temperature pin. In fact, the PNP transistor will be chosen with the higher β possible, but this will certainly create an asymmetry between emitter and collector current so that the theoretical value differs from the real one.

Finally, the ”on” resistance from the multiplexer has to be measured for a 12V supply voltage in order to adjust the first resistor of the series connected to it. The utility of the output voltage possibilities around 3.5V has to be checked because the PCB implementation of such a potentiometer is spacious and the controller circuit has to be repeated two times for the study (and 6 times for final design).

Chapter 4
Negative high voltage generation for detector bias

This fourth chapter will detail the design of a DC-DC converter in order to obtain a stable negative high voltage in order to bias the Silicon Drift Detector. First, a reminder of the purpose of having a high negative voltage is made and then, the specification of the converter is clearly defined. After, a theoretical explanation of the flyback operation is made. Then, the design is realized including the transformer and snubber circuit design. Finally, open-loop simulations are performed with evaluations of the influence of the parameters.

4.1 Purpose

When an X-Ray (incoming photon) hit the detector, ionization is produced in the high purity silicon. The corresponding electron-hole pair needs an electric field to drift to the small collection anode. This electric field is produced by the high negative voltage applied to a series of ring electrodes.

4.2 Specifications

4.2.1 Input

The input of the converter is the main DC power supply from the LUVMI-X rover:

- DC Nominal voltage: 28V
- Voltage range : 16-36V
- Stability: depending on LUVMI specification

4.2.2 Output

The output of the converter is the negative bias voltage for the detector chip. The needs are:

- DC Nominal voltage: -225V
- Maximal voltage range: -230 to -220V
- Maximal output current: 100 µA
- Ripple: 5mV P-P
- Stability: < 0.5V

4.3 Choice of the converter: Flyback

In order to ensure safety of the others embedded instruments on the rover, the output must be isolated from the input. This galvanic isolation will be achieved with a transformer. Since a transformer is used, multiple outputs are possible. The flyback topology offers this feature with many other advantages such as: very low power (<500W), high efficiency (> 70%), low part count (easy to implement and low cost) and the possibility to step-up the input voltage. It needs only one transistor drive. Another advantage compared to other isolated topologies is that the energy is directly stored in the transformer and there is no need for other inductor.

4.3.1 DCM or CCM

The Flyback can work in 2 distinct modes, depending on the design: Discontinuous Conduction mode (DCM) or Continuous Conduction Mode (CCM). In DCM, all the energy stored in the transformer is delivered to the secondary before turning on again. In CCM, this energy is not completely transferred. The current does not reach 0 before the next switching cycle.

DCM brings a series of advantages such as: smaller transformer, faster transient response, easy feedback or current loop compensation, no loss from reverse recovery on rectifier diode or low turn-on losses on the MOSFET. For these reasons, DCM allows lower power or high output voltage with low output current. This mode of operation requires higher peak currents and thus higher RMS ratings for the MOSFET and output capacitor, but also higher conduction losses in the transformer winding's.

DCM Flyback is thus chosen because the characteristics below match perfectly with the requirements.

4.4 Theory of operation

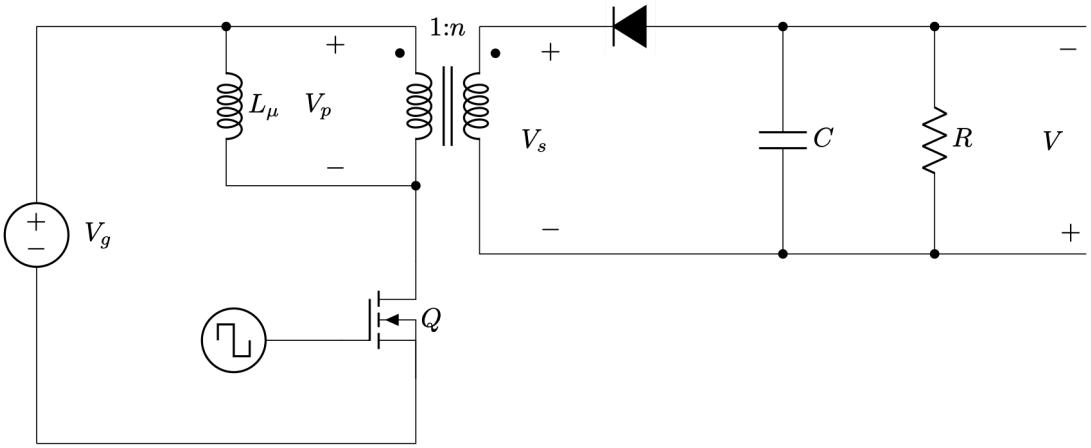

Figure 4.1 – Flyback converter with negative output

This flyback converter work in Discontinuous Conduction Mode.

4.4.1 Decomposition of the period

Each period of the PWM will be decomposed into 3 subintervals with ratio D_1, D_2 and D_3. The first one corresponds to the interval when the MOSFET in "on", the second corresponds to the time for the transformer to discharge its energy into the output and the third corresponds to the "reset" interval when no current is passing through the primary or secondary part of the transformer.

Subinterval 1

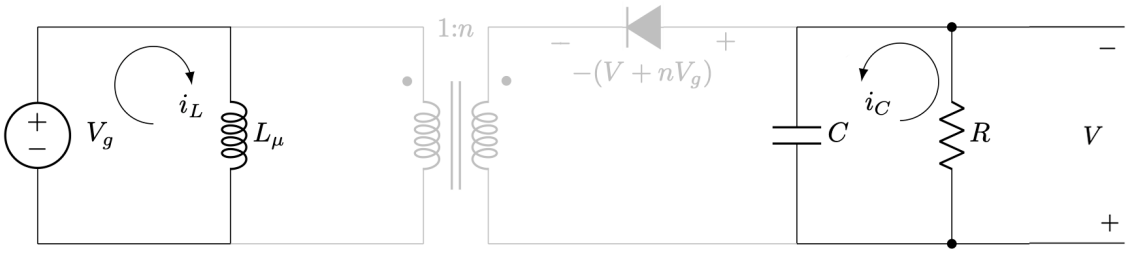

Figure 4.2 – Subinterval 1

When the MOSFET is on, the total input voltage appears to the primary side of the transformer (on the winding and on the magnetizing inductance). This voltage is transmitted to the secondary winding but no current can flow on the secondary side because of the reverse bias of the diode. All the input power will be stored thus in the magnetizing inductance. On the output side, the capacitor alone will provide current to the load and keep the voltage up.

Subinterval 2

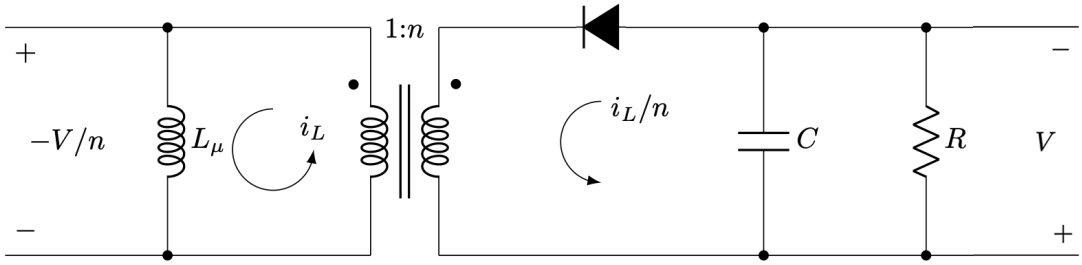

Figure 4.3 – Subinterval 2

When the MOSFET turns off (the source is cut off), the current stocked in the magnetizing inductance continue to flow and is transmitted to the secondary side with the diode forward biased. This secondary side is polarised by the output voltage (plus the diode junction voltage) so that the primary voltage jump to -V/n. The current flowing through the secondary charges the capacitor and flows through the load.

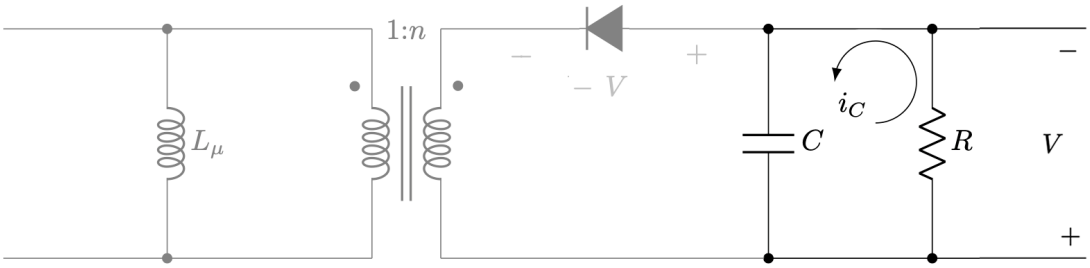

Figure 4.4 – Subinterval 3

Subinterval 3

When all the energy stored in the magnetizing inductance is drained, there is no more current flowing through the transformer (and through the diode). There is no potential difference at each side of the transformer. Once again, the capacitor alone will provide current to the load and keep the voltage up.

4.4.2 Flyback equations

Small ripple approximation

In a well designed converter, the output voltage ripple is small, so that the waveforms can be determined by ignoring it:

$$v(t) = V + v_{ripple}(t) \approx V \tag{4.1}$$

Average inductor voltage and capacitor current

When the converter operates in steady-state, the average inductor voltage and the average capacitor current are zero. This is called the volt-second and charge balance principles.

$$< v_L > = D_1 V_g + D_2 - \frac{V}{n} + D_3 0 = 0 \tag{4.2}$$

$$< i_C > = D_1 \frac{V}{R} + D_2(-\frac{< i_L >}{n} + \frac{V}{R}) + D_3 \frac{V}{R} = 0 \tag{4.3}$$

Steady-state DC solution

$$V = \frac{nD_1}{D_2} V_g \tag{4.4}$$

$$< i_L > = \frac{n}{D_2} \frac{V}{R} \tag{4.5}$$

but D_2 is unknown. Indeed, D_2 is a consequence and depends on D_1 which the variable driven by the PWM regulator.

Waveforms: The waveforms of this flyback converter in DCM are depicted in figure 4.5.

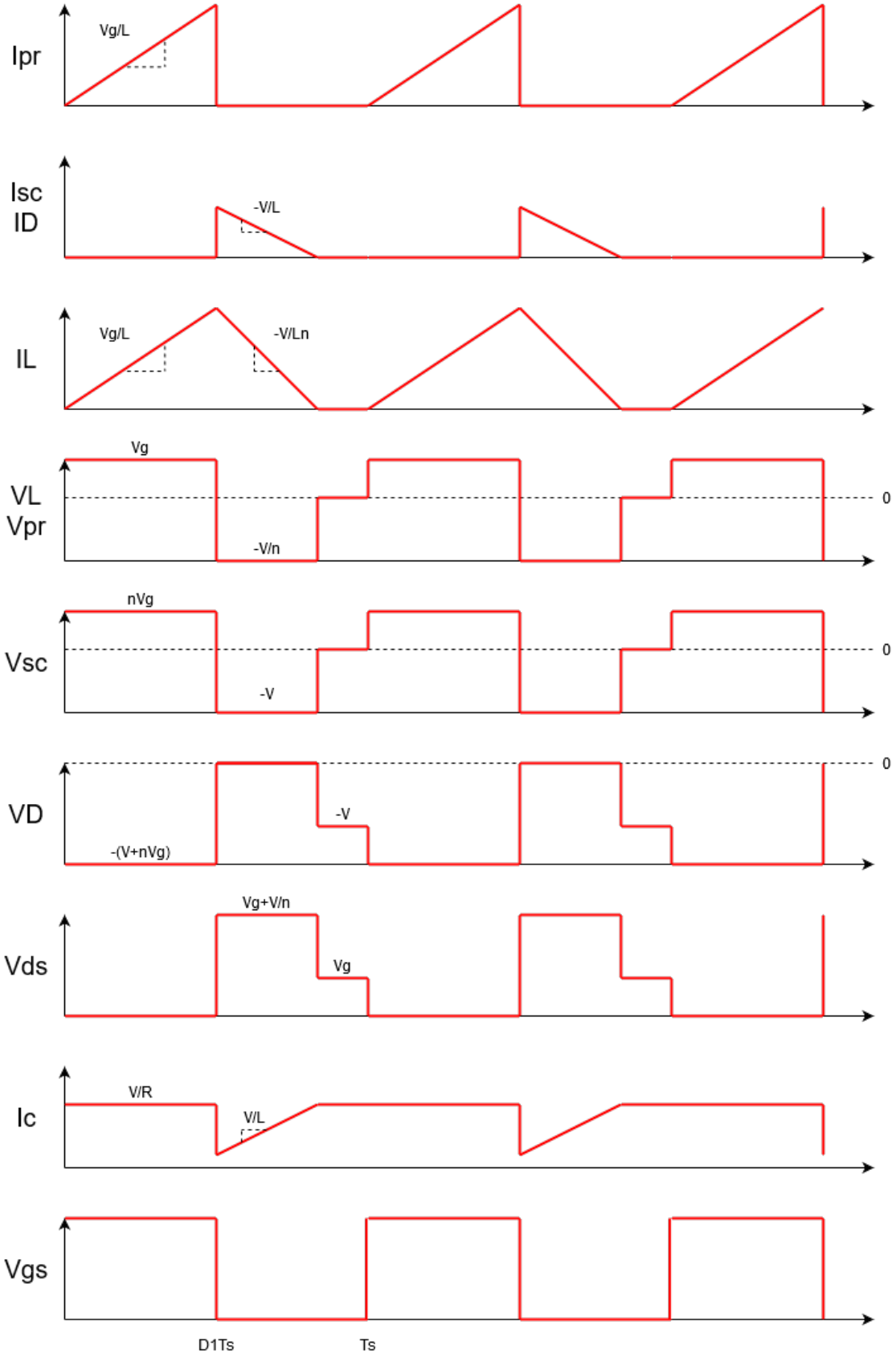

Figure 4.5 – Flyback waveforms

Peak current in the primary side of the transformer can be computed:

$$i_L(D_1T_s) = i_{pk} = \frac{V_g}{L}D_1T_s \tag{4.6}$$

From this peak current, an other way to compute average current in the magnetizing inductance of the transformer is found:

$$\begin{aligned} < i_L > &= \frac{1}{T_s}\int_0^{T_s} i_L(t)dt \\ &= \frac{1}{T_s}\frac{1}{2}i_{pk}(D_1+D_2)T_s \text{ (triangle area formula)} \\ &= \frac{V_g}{2L}D_1T_s(D_1+D_2) \end{aligned} \tag{4.7}$$

And equating (4.5) and (4.7), a new relationship is obtained:

$$\frac{n}{D_2}\frac{V}{R} = \frac{V_g}{2L}D_1T_s(D_1+D_2) \tag{4.8}$$

And now there are 2 equations ((4.4) and (4.8)) with 2 unknowns (V and D_2). The algebraic resolution is quite complicated, but can lead to an expression of the conversion ratio independent of D_2.

DCM vs CCM:

In order to have a discontinuous behaviour, some conditions can be evaluated. First, the current passing through the diode is at its minimum when the average inductor current is reduced by Δi_L. This current ripple is equal to the peak current (equation (4.6)) divided by 2. DCM is achieved when this current ripple is greater than the average current:

$$I < \Delta i_L \tag{4.9}$$

$$I < \frac{V_g}{2L}D_1T_s \tag{4.10}$$

Replacing I and V by the expression from the CCM flyback converter (equations (4.4) and (4.8) with $D_1 + D_2 = 1$):

$$\begin{aligned} \frac{nV}{D_2R} &< \frac{V_g}{2L}D_1T_s \\ \frac{n^2}{RD_2^2} &< \frac{T_s}{2L} \\ \frac{2n^2L}{RT_s} &< (1-D_1)^2 \end{aligned} \tag{4.11}$$

An expression of the form: $K < K_{crit}(D_1)$ is obtained for DCM with:

$$K = \frac{2n^2L}{RT_s} \tag{4.12}$$

$$K_{crit} = (1-D_1)^2 \tag{4.13}$$

This boundary between DCM and CCM modes is illustrated in figure 4.6.

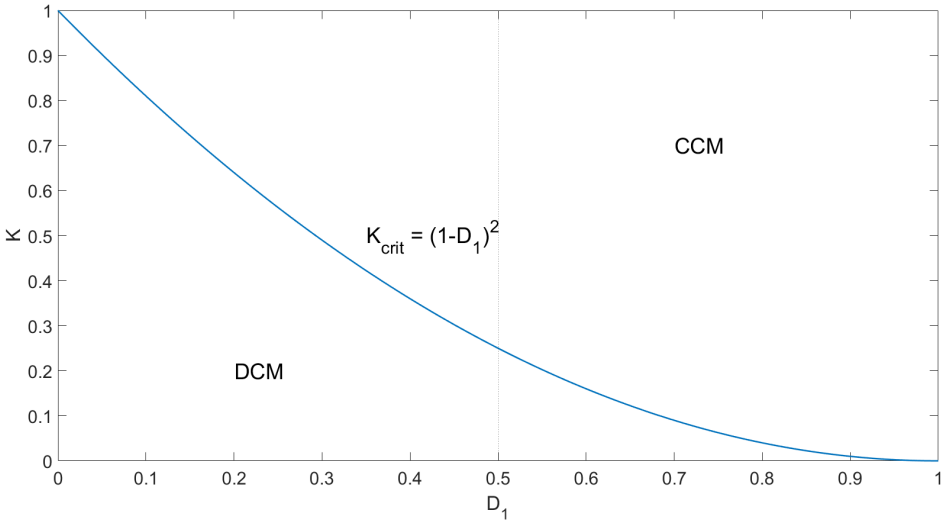

Figure 4.6 – DCM-CCM boundary

Power transfer: The power transfer in the transformer can be computed thanks to the magnetizing current and its peak value (equation (4.6)):

$$P = V * I = L\frac{dI}{dt} * I = L\frac{1}{2}\frac{dI^2}{dt} = \frac{LI_{pk}^2}{2}\frac{1}{T_s} \tag{4.14}$$

$$I_{pk} = \sqrt{\frac{2P}{Lf}} \tag{4.15}$$

but the peak current can also be expressed in term of D_2 by taking the discharging slope:

$$I_{pk} = \frac{V}{nL}D_2T_s \tag{4.16}$$

So the 2 relations appear:

$$\frac{1}{V_g}\sqrt{2PLf} = D_1 \tag{4.17}$$

$$\frac{n}{V}\sqrt{2PLf} = D_2 \tag{4.18}$$

Knowing the condition in order to have a DCM behaviour:

$$D_1 + D_2 \leq 1 \tag{4.19}$$

Thus, this condition on L is obtained:

$$L \leq \frac{1}{2Pf}(\frac{1}{V_g} + \frac{n}{V})^{-2} \tag{4.20}$$

4.5 Design of the flyback

4.5.1 Transformer

Reflected voltage First, the reflected voltage (VR) is computed. This is the voltage across the primary winding when the switch is turned off. The equation is based on the maximum duty cycle, which is active when the input voltage is minimized. At this condition, the assumption that the converter work at the boundary of DCM and CCM is made. In practice, for space applications, $D \leq 0.5$ in order to limit peak current.

$$D_{max} = \frac{VR}{VR + V_{g,min}} \tag{4.21}$$

$$VR = \frac{D_{max}}{1 - D_{max}} V_{g,min} = \frac{0.5}{1 - 0.5} 16 = 16V \tag{4.22}$$

Although fixed by the maximum duty cycle here, the reflected voltage can be chosen in other design. This choice will be the result of a trade-off between the MOSFET and the rectifier voltage stress. Indeed, this value is directly proportional to the turn ratio, so that a high VR will increase the diode stress but will decrease the MOSFET stress.

Primary peak current In order to find the primary peak current thanks to the power, the combination of equations (4.6) and (4.14) gives:

$$P_{in,max} = \frac{P_{out,max}}{\eta} = V_{out,max} I_{out,max} = 230 \times 100\mu = 0.023W \tag{4.23}$$

$$I_p = \frac{2P}{V_g D_1} = \frac{2P_{in,max}}{V_{g,min} D_{max}} = \frac{2 \times 0.023}{16 \times 0.5} = 5.75mA \tag{4.24}$$

Indeed, the efficiency of the converter looks to be maximized ($\eta \sim 1$). The maximum output current value must be adjusted with the current consumed by the voltage divider in the feedback loop.

Maximum primary inductance From equation (4.6):

$$L_{p,max} = \frac{V_{g,min} D_{max}}{I_p f} = \frac{16 \times 0.5}{5.75m \times 500k} = 2.7826mH \tag{4.25}$$

Turn ratio Under the same assumption (boundary CCM-DCM), the turn ratio can be computed:

$$n = \frac{N_s}{N_p} = \frac{V_{out} + V_D}{VR} = \frac{225 + 0.7}{16} = 14.10625 \tag{4.26}$$

Secondary current and inductance From this term, secondary peak current and secondary inductance can be found:

$$I_s = \frac{I_p}{n} = \frac{5.75m}{14.10625} = 407.62\mu A \tag{4.27}$$

$$L_{s,max} = L_{p,max} n^2 = 2.7826m \times 14.10625^2 = 553.699mH \tag{4.28}$$

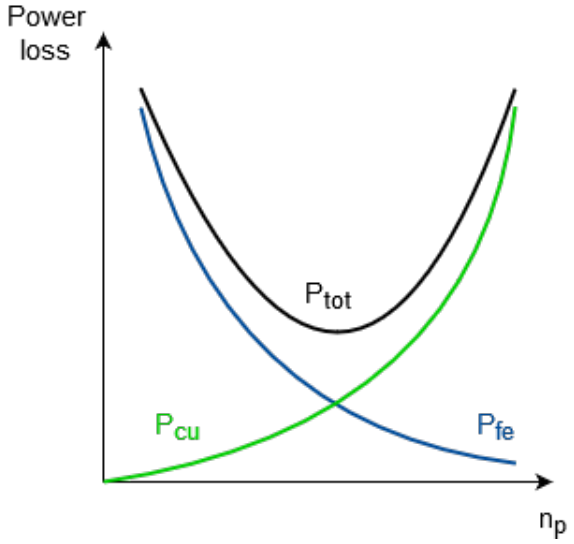

Figure 4.7 – Power losses in the transformer vs primary turn number

4.5.2 Number of turn optimization

The number of turns is a critical choice in order to minimize the power losses of the transformer. Indeed, a high number of turns will reduce magnetic losses, but will increase conduction losses. A compromise must thus be found, according to a lot of parameters such as: core choice, current flowing through the transformer, the value of the inductances, turn ratio and wire choice. This trade-off is illustrated in figure 4.7.

Core choice

In this step, knowing the values above, a magnetic core is selected. This core bring new parameters: effective area A_e, operating maximum flux density B_{max}, magnetic length l_m, exponent β, constant of proportionality depending on material K_{fe}, window area w_a and mean length turn MLT.

The primary peak current current can be related to the flux density by:

$$\lambda = L_p I_p = n_p A_e B \tag{4.29}$$

$$n_{p,min} = \frac{L_p I_p}{A_e B_{max}} \tag{4.30}$$

Core loss depends on flux density and thus on the primary number of turns. Manufacturers published data-sheets that contain plots of P_{fe} of the form:

$$P_{fe}(n_p) = K_{fe} B^{\beta} A_e l_m = K_{fe} (\frac{L_p I_p}{n_p A_e})^{\beta} A_e l_m \tag{4.31}$$

So this loss decreases with the increase of n_p. But increasing n_p will increase copper loss. The best compromise must be found in order to minimize total losses.

Copper loss First, 2 variables are introduced, α_p and α_s, which are respectively the fraction of window area allocated to primary or secondary ($\alpha_p + \alpha_s = 1$). For example, these parameters are illustrated in a classical core-type construction as in figure 4.8.

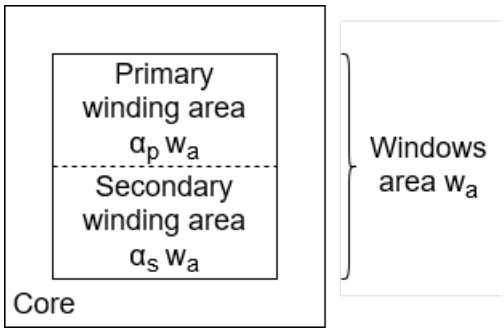

Figure 4.8 – Winding areas

Then, wire areas are found:

$$A_{w,i} = \frac{\alpha_i K_u w_a}{n_i} \text{ with } i = p, s \tag{4.32}$$

with K_u, the fill factor fixed to 0.4.

From these values, winding resistances can be computed:

$$R_i = \rho \frac{n_i (MLT)}{A_{w,i}} \tag{4.33}$$

with ρ the resistivity of the copper equal to 1.68×10^{-8}.

Copper loss in each winding is equal to:

$$P_{cu,i} = I_{i,rms}^2 R_i \tag{4.34}$$

The primary and secondary RMS currents are:

$$I_{p,rms} = I_p \sqrt{\frac{D_{max}}{3}} \tag{4.35}$$

$$I_{s,rms} = I_s \sqrt{\frac{1 - D_{max}}{3}} \tag{4.36}$$

Combining equations (4.32), (4.33) and (4.34), the total copper losses are:

$$P_{cu}(n_p) = P_{cu,p} + P_{cu,s} \tag{4.37}$$

$$= \rho \frac{n_p^2 (MLT)}{K_u w_a} \left(\frac{I_{p,rms}^2}{\alpha_p} + \frac{n^2 I_{n,rms}^2}{\alpha_s} \right) \tag{4.38}$$

$$n = \frac{n_s}{n_p} \tag{4.39}$$

The minimum is achieved when:

$$\alpha_p = \frac{I_{p,rms}}{I_{p,rms} + n I_{s,rms}} \text{ , } \alpha_s = \frac{n I_{s,rms}}{I_{p,rms} + n I_{s,rms}} \tag{4.40}$$

The trend of the curve of $P_{cu}(\alpha_p)$ is depicted in figure 4.9.

The expression of total losses is a function of the primary number of turns and have

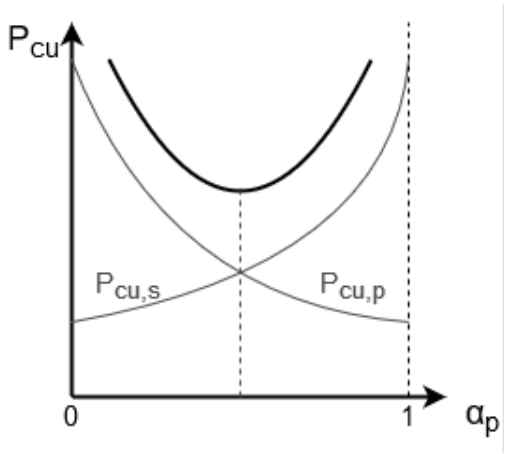

Figure 4.9 – Copper loss vs α_p

to be minimized. It is here a discrete optimization problem:

$$\min P(n_p) = P_{cu}(n_p) + P_{fe}(n_p) \tag{4.41}$$

$$\text{under the constraints: } n_p \geq n_{p,min} \tag{4.42}$$

$$n_p \in \mathbb{N} \tag{4.43}$$

4.5.3 Diode

The maximum voltage stress experienced by the diode is during D_1 when the input and the output voltage are maximum and the diode receives both (with turn ratio correction for input voltage).

$$V_D = V_{out,max} + nV_{in,max} \tag{4.44}$$

4.5.4 Output capacitor

First, the output ripple specification must be respected. This is achieved with a maximum impedance (at the switching frequency) of:

$$Z_{c,max} = \frac{V_{out,ripple}}{I_s} \tag{4.45}$$

Second, the RMS capacitor current is:

$$I_{c,rms} = \sqrt{I_s^2 - I_{out}^2} \tag{4.46}$$

Finally, the minimum capacitance value is given by:

$$I = C\frac{dV}{dt} \tag{4.47}$$

$$C_{out,min} = \frac{I_{out,max}}{fV_{out,ripple}} \tag{4.48}$$

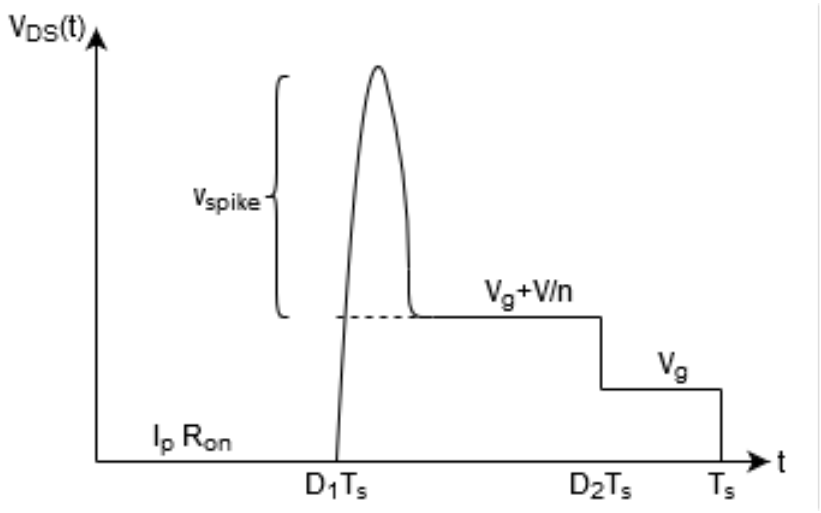

Figure 4.10 – MOSFET voltage without snubber

4.5.5 MOSFET

V_{DS} is calculated by:

$$V_{DS,max} = V_{g,max} + \frac{V}{n} + V_{spike} \tag{4.49}$$

but V_{spike} is difficult to estimate. A snubber circuit will be designed to attenuate this value.

I_{DS} will be rounded twice the value of I_{pk}.

4.5.6 Snubber circuit

A transformer present always a leakage inductance that can be modelled as a inductance in series with the magnetizing inductance (and thus with the MOSFET): L_{lk}. When the MOSFET turns off, it interrupts current flowing through L_{lk} and this leakage inductance produces a voltage spike as described in figure 4.10.

$$v_{spike}(t) = L_{lk}\frac{di_p}{dt} \tag{4.50}$$

The snubber circuit is an RC parallel circuit connected to the primary of the transformer with a diode as illustrated in figure 4.11. This setup provides a path for i_p to flow when the MOSFET turns off.

In a good, carefully wound transformer, it may be possible to achieve a leakage inductance $L_{lk} = 3\%L_m$.

The average power transferred from L_{lk} to the snubber circuit (and to C_s) is:

$$P_{lk} = \frac{L_{lk}I_p^2 f}{2} \tag{4.51}$$

A safe margin of 80% of $V_{DS,max}$ is chosen to be the limit. Then, the snubber voltage will be:

$$V_s = 0.8 * V_{DS,max} - \frac{V}{n} \tag{4.52}$$

Such that the voltage spike is clamped as depicted in figure 4.12. So R_s is chosen to

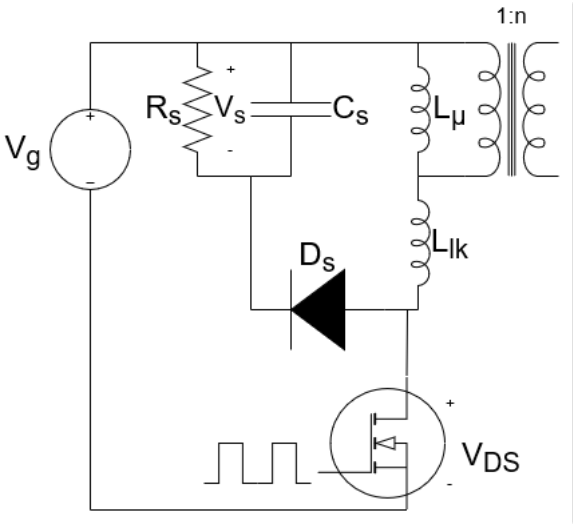

Figure 4.11 – Snubber circuit

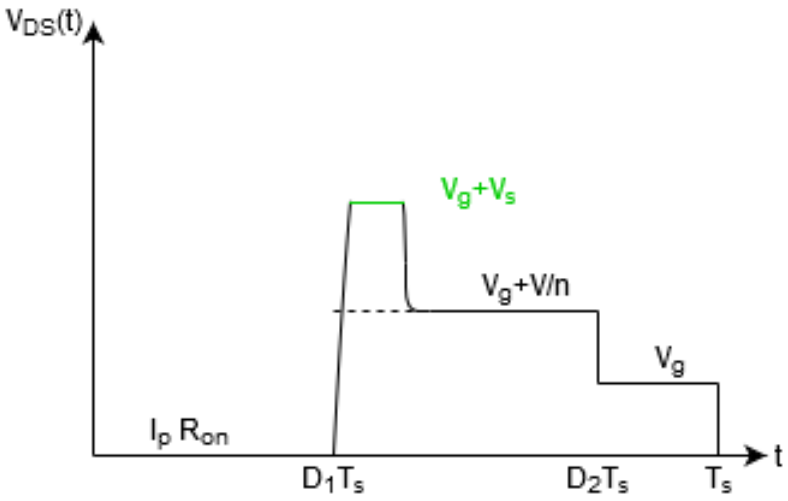

Figure 4.12 – MOSFET voltage with snubber

dissipate the leakage power.

$$R_s = \frac{V_s^2}{P_{lk}} \tag{4.53}$$

Then, a large C_s is used so that $v_s(t)$ has negligible ripple:

$$C_s >> \frac{T_s}{R_s} \tag{4.54}$$

The value of C_s may be selected between 100pF to 4,7nF, the energy stored in this capacitor will be discharged and refreshed by R_s quickly during each switching cycle.

4.6 Simulations

The simulations were performed using LTSpice XVII.

The load resistor is assumed to be ideal (no tolerance or power rating) and the output capacitor too (no voltage/current rating, no equivalent series/parallel resistance, capacitance or inductance). The MOSFET is chosen in the library with a sufficient V_{ds} (80V): BSC047N08NS3. The diode is simulated with its basic model too. The transformer is made of 2 ideal inductors (no series or parallel resistance nor parallel capacitance) coupled with a single mutual inductance (no leakage). The pulse is generated artificially.

4.6.1 Nominal operating point

The principle of the next simulation is to show the influence of the parameters on the circuit behaviour. In order to do that, a nominal operating point is determined and the parameters of the Flyback are changed to observe their influence. Indeed, in DCM, the output current depends on the duty cycle, the load resistance, the switching period, the transformer parameters and of course, the input voltage.

When the closed-loop will be designed (in the form of an Integrator), the enslavement will compensate reasonable deviation from this operating point. In fact, the compensation loop reduces the peak current by decreasing the duty cycle if the output voltage exceeds the set-point (and inversely). If the parameters are oversized, it is going to be technically difficult to obtain very precise duty cycle correction.

The frequency is fixed at 500 kHz. Then, a load of 10k ohms is chosen in order to have sufficient peak current. From that value, the power to be injected in the converter can be computed and the peak current magnitude found (equation (4.14)). From equation (4.6), the primary inductance magnitude is found too. The turn ratio is chosen according to an existing transformer with these 2 values as a reference. The output capacitor minimum value is described by equation (4.48) where $I_{out,max}$ is deduced from the load. Finally, the Flyback scheme is illustrated in figure 4.13.

Waveforms

As can be seen in figure 4.14, the DCM is achieved and the waveforms are close to the theoretical ones depicted in figure 4.5. The differences are caused by the MOSFET real parameters such as a on resistance which decreases the peak current and its gate capacitance which determines the switching speed.

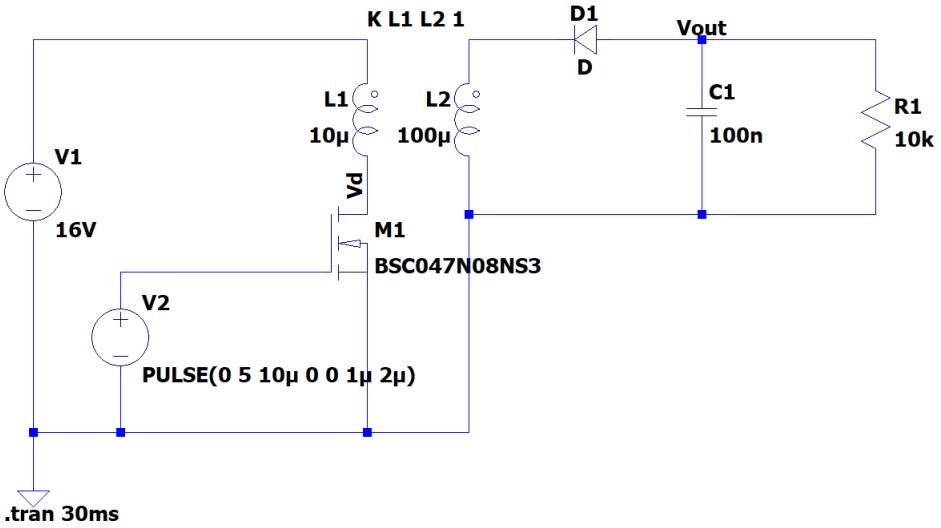

Figure 4.13 – Nominal operating point simulation schematic

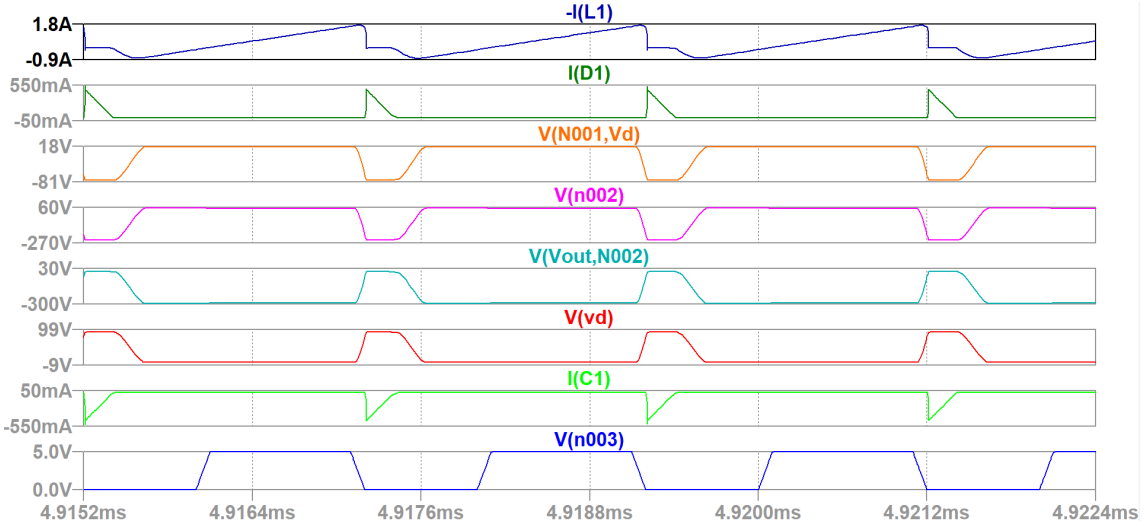

Figure 4.14 – Simulated waveforms for the Flyback

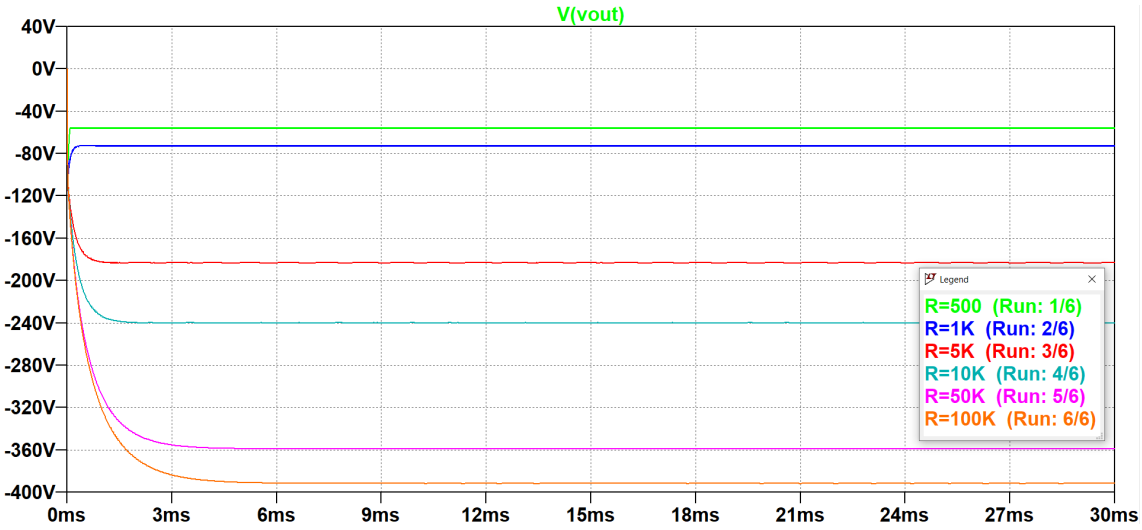

Figure 4.15 – Output voltage with different R values

Load influence

Several resistor values were tested to see their influence on the output voltage in steady-state. Other parameters stay fixed by the nominal operating point. The minimum resistor value is 400 ohms to ensure DCM by equation (4.11). The results are shown in figure 4.15.

The higher the resistance is, the higher the negative output voltage is too. For a 10k ohm resistor, an output voltage of -240V is obtained. When compared to other values, a proportional relationship can be found: $V_{out} \propto \sqrt{R}$.

Switching period influence

The frequency will act on the output voltage but also on the peak current, the output capacitor requirements (for a fixed ripple) and the snubber circuit. According to equation (4.11), minimum switching period is 80ns (maximum frequency of 12.5MHz) to ensure DCM operation. Several T_s are tested and the results are presented in figure 4.16.

The output voltage increases with the switching period (decreases with frequency). As expected, the output ripple increases too, because of the fixed value of the output capacitor. Once again, a proportional relationship between output voltage and switching period is found: $V_{out} \propto \sqrt{T_s}$.

Duty cycle influence

The only parameter on which the compensation loop will act is the duty cycle. It determines the amount of time when the MOSFET conducts. A maximum value of 0.5 is usually used in space in order to limit peak current. Values between 0.1 and 0.5 are tested and the corresponding simulation is shown in figure 4.17.

When the duty cycle increases, the negative voltage increases too. A gap is clearly observed between 0.3 and 0.4. This result in the complex proportional relation between D and V_{out}.

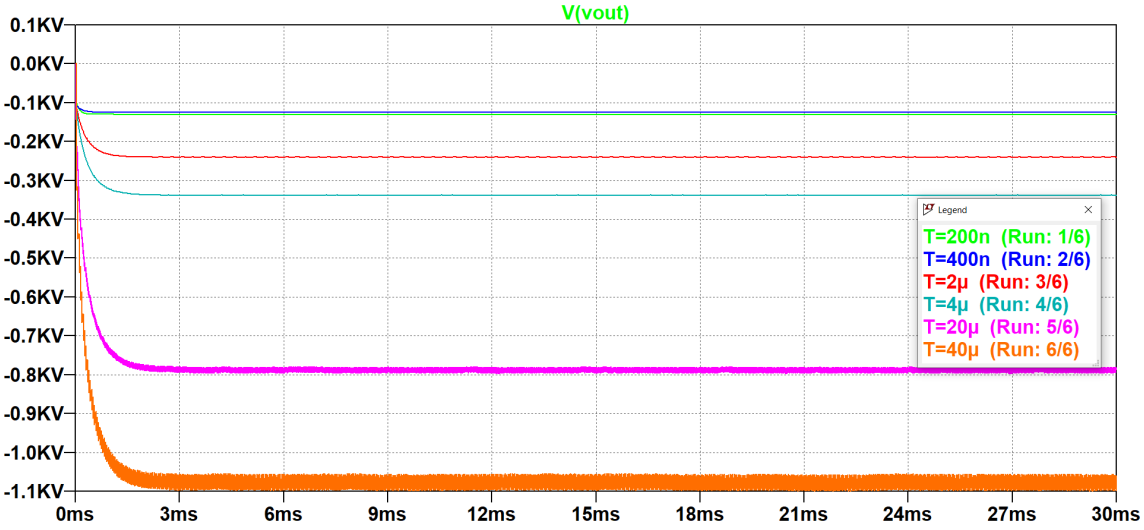

Figure 4.16 – Output voltage with different T_s values

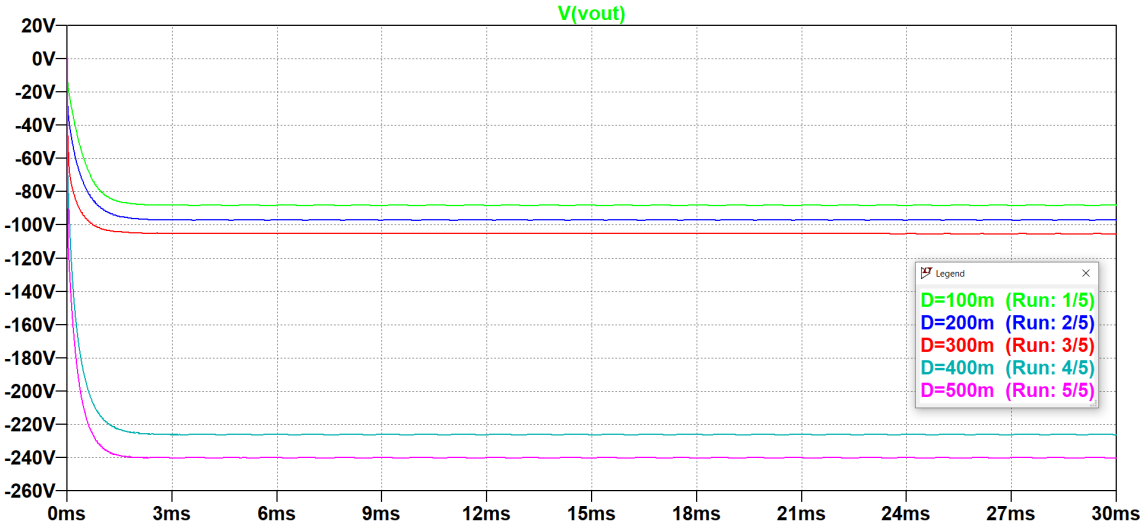

Figure 4.17 – Output voltage with different D values

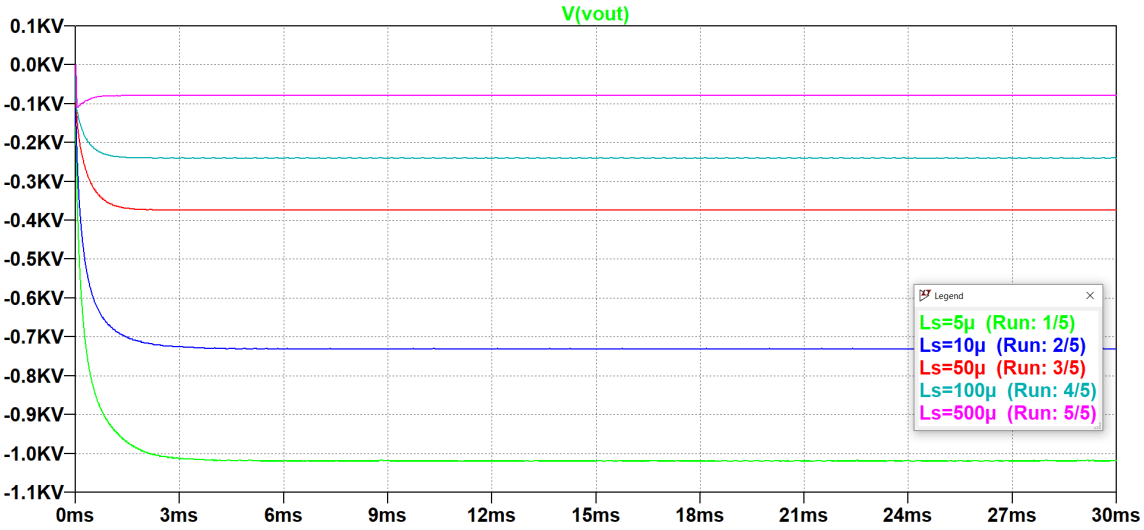

Figure 4.18 – Output voltage with different inductances values (same n)

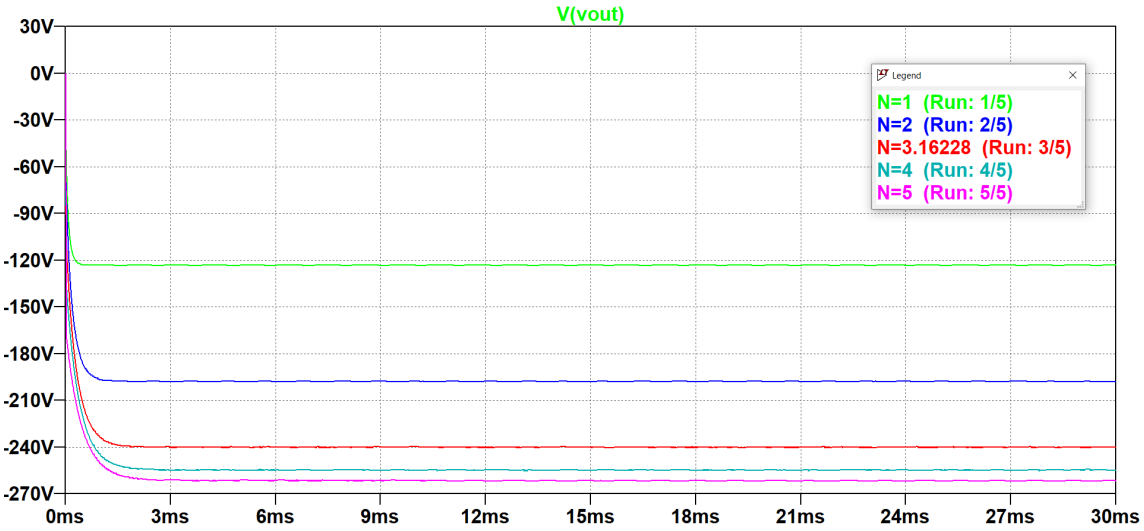

Figure 4.19 – Output voltage with different turn ratio (L_s modified)

Inductance influence

The inductor values are changed respectively with the same turn ratio ($10L_p = L_s$). With equation (4.11), the secondary inductance can not exceed 2.5 mH. Simulations with a range of values between 5 and 500 µH are performed and the corresponding curves are depicted in figure 4.18.

The negative output voltage increase in reverse with the inductance value. Once again, a new proportionality relation can be expressed by measuring the different values: $V_{out} \propto \frac{1}{\sqrt{L_s}}$.

Turn ratio influence

To modify the turn ratio, 2 options are possible: modifying the primary inductance or the secondary. The figure 4.19 presents the results when modifying secondary inductance and the figure 4.20 presents the results when modifying primary inductance.

As can be seen, the output voltages are higher for same turn ratio when we modify the

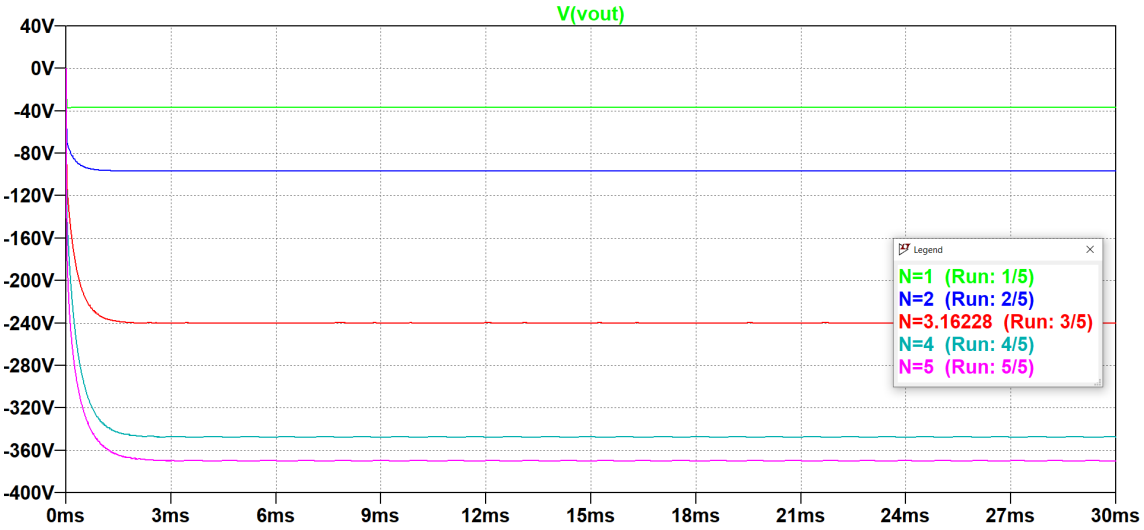

Figure 4.20 – Output voltage with different turn ratio (L_p modified)

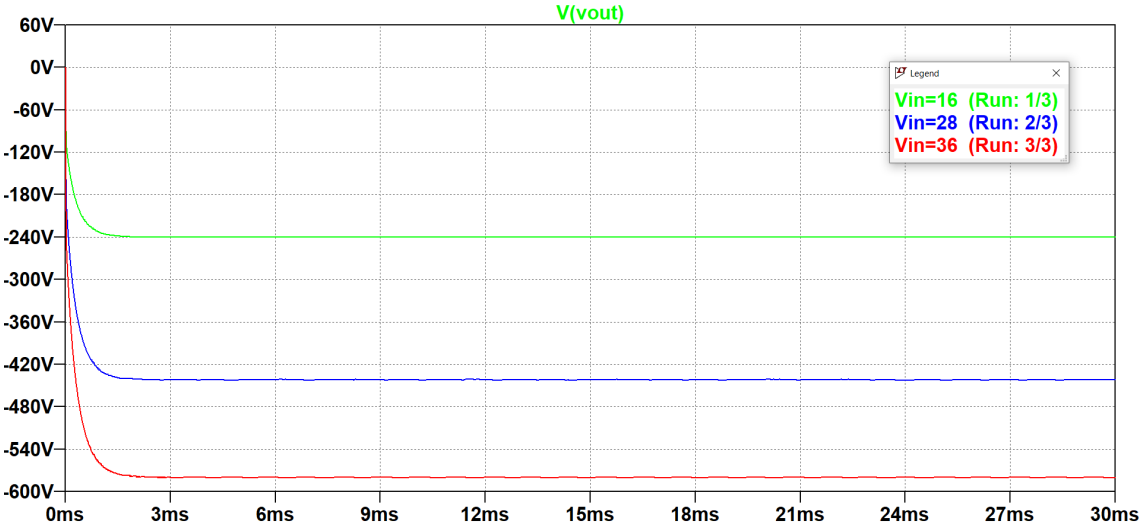

Figure 4.21 – Output voltage with different input voltages

primary instead of the secondary. Indeed, the secondary will influence the discharging time while the primary influence the peak current and the energy stored in the transformer. Generally, the voltage increases with n but a damping is observed from $n = 3 \sim 4$.

Input voltage influence

The minimum, nominal and maximum voltage values are tested. The result is presented in figure 4.21.

These results prove that the negative output voltage is directly proportional to the input voltage: $V_{out} \propto V_{in}$.

4.7 Conclusion

In this chapter, the concept of the DCM Flyback converter was clearly explored. This DC-DC converter produces a negative high voltage from the LUVMI-X power supply battery

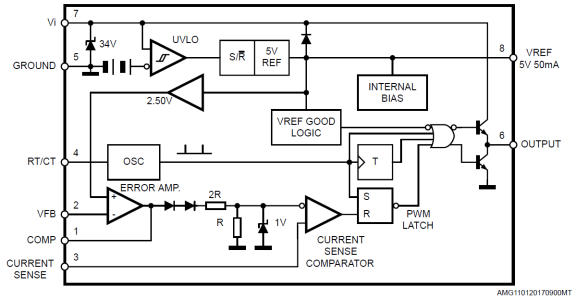

Figure 4.22 – Block diagram of ST1845 PWM controller

to stabilize the bias of the Silicon Drift Detector.

First, a clear specification for the converter was described. After discussing the choice of the topology, the principle of operation of a Flyback converter was demonstrated. Then, a design procedure accompanied by an Excel spreadsheet to tune the parameters has been described. An extra feature, the snubber circuit, was designed to ensure the MOSFET safety. Simulations around a nominal operating point were performed in order to see the influence of each parameter in open-loop on the output voltage (with other values fixed). These simulations respect the theoretical equations listed just before.

Closed-loop design

This chapter is ended by open-loop simulations. Naturally, the next step is the closed-loop design associated with a compensation mechanism. This setup will drive the duty cycle. The feedback will be given by a voltage divider[1] followed by a voltage inverter in order to compare it to a reference set-point. The error will be integrated so that the response will be closer to this set-point after a few switching cycles. This regulation is the key point of the stability of the output voltage. Even if an event changes one of the parameters (battery discharging, change in load...), the negative high voltage will stay as stable as possible.

In commercial applications, PWM controllers present often these pins:

- A feedback pin which is the inverting input of the error amplifier. It is normally connected to the switching power supply output through the resistor divider (and inverter for negative output).
- A compensation pin which is the output of the error amplifier used for loop compensation.
- A current sense pin which is connected to a voltage proportional to inductor current. This information is used to terminate the output switch conduction.
- A pin to control the oscillator frequency.
- The ground.
- The output pin which is the PWM send to the MOSFET.

A corresponding block diagram from ST1845 is presented in figure 4.22. Some commercial integrated circuits offer also the possibility to switch between modes and thus offers a larger range of power (from zero to the maximum) but this elementary system is not suitable for that.

[1]The current passing trough this voltage divider must be taken into account for the power computation.

Chapter 5
Final conclusion

The goal of this thesis was to design the power supply for an X-Ray Fluorescence instrument. This technology is mainly composed of a series of X-Ray sources and one Silicon Drift Detector, the actual state of the art in energy-dispersive analysis for XRF. The physical principles of these elements were discussed in the Introduction chapter. In this chapter, a clear specification for the power supply was also defined. The power supply is basically composed of 3 parts.

First, an analog Peltier cooler regulator was designed. The Thermo-Electric Cooler (TEC) is used to maintain the detector temperature as stable as possible during the measurements. The first task was to simulate a Peltier cooler in LTSpice. The results are close to the reality. This Peltier element is driven by current. The second task was to implement an analog current source. Once done, the choice of an analog PID controller topology to control the current was made. This controller passes the measured error into three terms in order to have a nice response on the temperature measurement. Finally, the simulations were performed to adjust the PID parameters to obtain a desired reaction to a perturbation.

Second, a self-switching voltage source was implemented to control the X-Ray generators. Indeed, the two sources are thermally cycled to have a continuous flux of X-Rays. The radiations are produced by a pyroelectric crystal (oscillating between heat and cool phase). After getting a good definition of the source parameters and requirements, a complete design was made. This design is based on an analog Schmitt trigger. This setup offers the possibility to have two thresholds on the temperature while using one operational amplifier (one more for the pre-amplifying stage). In order to have a versatile output, a variable gain amplifier stage was added to the design. The goal is to control with digital inputs the output voltage level. Final simulations confirm the suitable behaviour for this particular application.

Third, a DC-DC converter was studied in order to generate a high negative voltage. This HV is used by the SDD to drift the charge carriers created by X-Rays in the material to the collection electrode. This voltage has thus a high need in stability in order to perform precise measurements. The choice of the Flyback topology was easily made and the DCM behaviour chosen. The first step of the study was to understand the theory of operation of such a converter. Then, a design method was implemented (with an Excel spreadsheet). Finally, simulations were performed to verify the theory and to observe the influence of the parameters on the output voltage.

For each part, a discussion was made to discuss the next steps of the developments (practical implementation for the 2 first parts and closed-loop design for the last one). An important step in the design of a power supply is also the power consumption and an analysis of efficiency. This must be performed when the practical implementation will start.

Electronic design in space implies a series of challenge which can be found in this thesis. Firstly, a limited list of available components for space is taken as a standard (EPPL). Secondly, space environment is harsh, mainly due to temperature and radiations. A special care must be made to ensure that the circuits are as simple as possible. Digital signals and components are more likely to fail and thus are to be avoided. Finally, space missions are very unique and important so that the quality level is at its maximum. Efficiency, safety and reliability are the watchwords in space developments.

As a result, this work represents a strong basis for practical implementation in the near future. Most of the requirements from the initial specification are full filled. The frame is well posed and the challenges are clearly described.

Bibliography

[1] C.K. Alexander and M.N.O. Sadiku. *Fundamentals of Electric Circuits*. McGraw-Hill, 2009.

[2] Amptek. *Miniature X-Ray Generator with Pyroelectric Crystal*. COOL-X. URL: https://www.amptek.com/-/media/ametekamptek/documents/products/coolx.pdf.

[3] K.J. Åström and R.M. Murray. *Feedback Systems: An Introduction for Scientists and Engineers*. Princeton University Press, 2010.

[4] James Brownridge and Sol Raboy. Investigations of pyroelectric generation of x rays. *Journal of Applied Physics*, 86(1), July 1999.

[5] Alain Carapelle. *Réalisation d'un spectromètre à fluorescence X portable*. PhD thesis, Université de Liège, Octobre 2013.

[6] Alain Carapelle, Jean-Marc Defise, David Strivay, and Henri-Pierre Garnir. Handheld modern computer brings new features to portable x-ray fluorescence coating thickness measurement device. *Computer Physics Communications*, 182:1304–1306, 06 2011.

[7] T.C. Carusone, D. Johns, and K. Martin. *Analog Integrated Circuit Design*. Analog Integrated Circuit Design. Wiley, 2011.

[8] ESA Publications Division. *Electrical, Electronic and Electromechanical (EEE) Components*. European Coordination for Space Standardization, April 1996. ECSS–Q–60A. URL: https://ecss.nl/standard/ecss-q-60a-electrical-electronic-and-electromechanical-eee-components-19-april-1996/.

[9] eCircuit Center. *Opamp Current Source*, 2002 (accessed 2020-02-17). URL: http://www.ecircuitcenter.com/Circuits/curr_src1/curr_src1.htm.

[10] eCircuit Center. *The Op Amp PID Controller*, 2004 (accessed 2020-02-26). URL: http://www.ecircuitcenter.com/Circuits/op_pid/op_pid.htm.

[11] Electronique.aop.free.fr. *Comparateur Trigger de Schmitt non-inverseur*, (accessed 2020-01-12). URL: http://electronique.aop.free.fr/AOP_sature/3_comparateur_schmitt_noninv.html.

[12] R.W. Erickson and D. Maksimovic. *Fundamentals of Power Electronics*. Springer US, 2012.

[13] ESA. *Technology Readiness Levels (TRL)*, 2017 (accessed 2020-05-29). URL: https://www.esa.int/Enabling_Support/Space_Engineering_Technology/Shaping_the_Future/Technology_Readiness_Levels_TRL.

[14] European Space Agency. *EUROPEAN PREFERRED PARTS LIST (EPPL)*, June 2019. ESCC/RP/EPPL007-38 (REP 007). URL: https://escies.org/webdocument/showArticle?id=965&groupid=6.

[15] Hiroyuki Ida and Jun Kawai. Portable x-ray fluorescence spectrometer with a pyroelectric x-ray generator. *X-Ray Spectrometry*, 34:225–229, 2005.

[16] W.G. Jung. *IC Op-amp Cookbook*. Prentice Hall PTR, 1997.

[17] Jakub Karczewski, T. Miruszewski, Beata Bochentyn, and Bogusław Kusz. Determination of ionic conductivity in the bi-si-o and pb-si-o glasses. *Materials Science-Poland*, 35, 12 2017. doi:10.1515/msp-2017-0102.

[18] Michael J. Sampson Kenneth A. LaBel. When is qualification not qualification? NASA Electronic Parts and Packaging Program (NEPP). URL: https://nepp.nasa.gov/workshops/etw2011/submissions/talks/Thursday/0830%20-%20When%20is%20Qualification%20not%20Qualification.pdf.

[19] Gwan-Bon Koo. Design guidelines for rcd snubber of flyback. Application Note AN4147, Fairchild Semiconductor, 2005.

[20] Mirion Technologies. *X-PIPS™ Detector (SDD)*, Oct. 2016. SXD30M-500-CM-PA. URL: https://mirion.s3.amazonaws.com/cms4_mirion/files/pdf/spec-sheets/c48107_sxd30m-500-cm-pa_super_spec_2.pdf?1559672928.

[21] ESA Requirements and Standards Division. *Derating - EEE components*. European Coordination for Space Standardization, Oct. 2011. ECSS-Q-ST-30-11C Rev 1. URL: https://ecss.nl/standard/ecss-q-st-30-11c-rev-1-derating-eee-components-4-october-2011/.

[22] RMT Ltd. *Thermoelectric Cooling Solutions*, 2019. 2MC04-039-XX/Z2. URL: http://rmtltd.ru/datasheets/2mc04039.pdf.

[23] Allan A. Saliva. Design guide for off-line fixed frequency dcm flyback converter. Design Note DN 2013-01, Infineon Technologies North America (IFNA) Corp., 2013.

[24] A.S. Sedra, D.E.A.S. Sedra, K.C. Smith, and P.E.K.C. Smith. *Microelectronic Circuits*. Oxford series in electrical and computer engineering. Oxford University Press, 1998.

[25] Giridharan Shanmugavel. Fly-back converter, ccm vs dcm. Maxim Innovation Delivered. URL: https://www.icbanq.com/icbank_data/online_seminar_image/Flyback_CCMVsDCM_Rev1p2.pdf.

[26] Global Sino. *Silicon Drift EDS Detectors (SDDs)*, 2006 (accessed 2020-05-25). URL: https://www.globalsino.com/EM/page2532.html.

[27] Sonelec-Musique. *Electronique - Réalisations - Potentiomètre numérique 001*, 2010 (accessed 2020-02-27). URL: https://www.sonelec-musique.com/electronique_realisations_pot_num_001.html.

[28] Space Applications Services NV/SA. *LUVMI: A Mobile Platform for Lunar Exploration & Experiments*. URL: https://www.spaceapplications.com/wp-content/uploads/2019/05/2-product-sheet-luvmi.pdf.

[29] Spi. *LIEGE Science Park*, 2011 (accessed 2020-06-03). URL: http://www.liegesciencepark.be/fr.

[30] B.G. Streetman and S. Banerjee. *Solid State Electronic Devices*. Prentice Hall series in solid state physical electronics. Prentice Hall, 2000.

[31] ULiège. *Centre Spatial de Liège*, 2018 (accessed 2019-10-10). URL: `https://www.csl.uliege.be`.

[32] P. Vanderbemden. *Analyse et conception des systèmes de mesures électriques*. CdC FSA asbl, 2017-2018.

[33] B. Vanderheyden. *Electronique analogique*. CdC FSA asbl, 2017-2018.

[34] R.M. Kubova V.I. Kubov, Y.Y. Dymytrov. Ltspice-model of thermoelectric peltier-seebeck element. *2016 IEEE 36th International Conference on Electronics and Nanotechnology (ELNANO)*, April 2016.

[35] A. Vladimirescu. *The SPICE Book*. Wiley, 1994.

[36] Wikipedia. *Wikipedia, the free encyclopedia*, (accessed 2020-01-06). URL: `https://www.wikipedia.org/`.

[37] T. Wikipedians. *An introduction to electronics*. The Art of Electronics. PediaPress GmbH, 2011.

[38] T. Wildi. *Electrical Machines, Drives, and Power Systems*. Prentice Hall, 2002.

[39] James Wilson. *170 V output flyback DC-DC converter*, 2020 (accessed 2020-04-26). URL: `https://hackaday.io/project/170962-170-v-output-flyback-dc-dc-converter`.

Appendix A
Internship: Centre Spatial de Liège

A.1 Introduction

This master thesis has been realized in the frame of an internship of 80 days at the Centre Spatial de Liège. This appendix will present a non-technical analysis of this spatial research center.

First, the history of the company will be described. Then, a presentation of the CSL will be performed trough its situation, its organization, etc. Finally, succinct descriptions of relevant projects with emphasis on analog and signal processing aspects will be presented.

A.2 History

At the Institute of Astrophysics of the University of Liège, first space activities were experiments on board rockets. At the beginning, Professor André Monfils was leading a little group of people in this Institute. These researches take place in the 60's when satellites were not yet available in Western Europe. After a few years, this group was called IAL-Space. Firstly, simulations of artificial comet and observations of the polar auroras were performed. Secondly, when satellites were available, IAL participates in the construction of various instruments for observing the stars, but also testing these equipment's under space conditions such as very low pressures and very low temperatures. The projects were leaded in the frame of well-known organisations: first the COPERS (Commission Provisoire d'Etudes et de Recherches Spatiales) and then the ESRO (European Space Research Organization) which is the predecessor of the ESA, the European Space Agency.

In 1992, when Pr. Monfils retired, IAL-Space changes its name and become the Centre Spatial de Liège. Professor Claude Jamar, a close collaborator of Pr. Monfils, will succeed at the head of the company for 50 years. From the beginning, the small group of a few people has grown and becomes a group of about 100 engineers, physicists and technicians.

The trust relationship with ESA grows with the years. Indeed, numerous missions developed largely by ESA (and to a lesser extent by NASA) will follow one another at the CSL such as cosmos, earth and its atmosphere or meteorology observations.

Figure A.1 – Liège in Europe [29]

A.3 Research center

The Centre Spatial de Liège (CSL) is an applied Research Center owned by the University of Liège, focused on design, integration and calibration of space observation instruments. CSL also operated a highly specialized environmental test center to support ESA programs as well as space industry and regional companies. CSL employs about 100 highly skilled employees within its Liège Science Park location.

A.3.1 Situation

CSL is located at Avenue du Pré-Aily, 4031 Angleur in the heart of the Liège Science Park. It is a specialized mixed economic activity park intended for Hi-Tech companies which have a link with the University of Liège.

Liège is a transborder location at the heart of Europe and have a good connectivity in term of transportation. Firstly, the Guillemins train station welcomes express train such as Thalys, Eurostar or ICE. Secondly, the port of Liège (on the Meuse) is the third most important river port in Europe. Thirdly, Liège airport is the first cargo hub in Belgium (7th in Europe) and is the leader in tailor-made solutions for transport. Finally, the city is surrounded by several European highways such as E40, E42 or E25. This advantageous location is illustrated in figure A.1.

CSL, as a research center, take part of the Science park policy which gives privileged access to research. University of Liège is the principal actor with 471 research units in all fields, 20 top-level interdisciplinary research centers (such as CSL) and relations with other companies. Indeed, the University has contacts with more than 600 Belgian and foreign companies, which represent a 150 million euros turnover in the industry (including 100 spin-offs).

A.3.2 Organization

Structure

The CSL is a research department of the University of Liège but has the structure of a private company.

Its executive committee is actually composed of three persons: Michel Bogaerts, Chief Financial & Human Resources Officer and Chief Executive Officer (ad interim), Serge Habraken, Director of Academic & Scientific Affairs and Emmanuel Janssen, Head of Product assurance/Safety. On the management side, there is also an Operational Excellence Coordinator (Jean-Yves Plesseria) and a Project Management Office Manager (Benoît Marquet).

Programs The CSL has four main programs:

- **Space tests**, headed by Christophe Grodent. The center is one of the key European test center for qualifying space instruments, sub-units or complete satellites.
- **Space systems**, headed by Philippe Bouchez. CSL creates, gathers, adjusts, calibrates and/or tests observation instruments and significant sub-frameworks able to work in a harsh domain, so as to serve the requests of the space science.
- **Technology Partnerships**, headed by Joseph Bernier. Beginning from know-how originating from Space Projects, this program offers services of R & D support and training, in space or other industrial domains.
- **Scientific Space Systems**, headed by Serge Habraken. This program is centered around the space instrumentation in close connection with the Scientists (principally Astrophysicists).

Labs In order to achieve its missions, CSL is composed of several advanced labs:

- **Surfaces Engineering**, headed by Karl Fleury. This lab controlled surface treatments dependent on deposit coatings, ion beam figuring, reactive plasma etching, surface micro texturing and related metrology.
- **Thermal & Mechanical Engineering**, headed by Jean-Yves Plesseria. These skills of the CSL initially developed to help its historical activities; design and integration of space instruments, just as operation of its unique set of environmental test facilities.
- **Test Facilities**, headed by Isabelle Tychon. CSL performs different qualifications on space instruments or equipment by submitting them to environmental space conditions.
- **Electronics**, headed by Nicolas Martin. This laboratory grown through the steady need to carry innovative answers to the issues created by the space condition and by the lasting solicitation of the space instruments to accomplish better signal to noise resolutions. The internship which is the frame of this thesis has been realised in this lab.

- **Optical design & Metrology**, headed by Yvan Stockman. The two main fields are space optical systems and optical metrology. The lab has a secular action in the design, development, integration and calibration of space optical systems as for astronomy than for earth observation purposes.
- **Lasers & NDT**, headed by Marc Georges. The capabilities of the group are historically fixated on laser metrology system developments, from research to pre-industrial prototyping and applications.
- **Signal Processing**, headed by Anne Orban. CSL exercices on radar imagery processing have started for twenty years and brought about the production of the "Space Environment and Remote Sensing Group".

Of course, all these units are interacting with each other in numerous projects and missions.

Buisness model

The CSL is a research center owned by the University of Liège. But it acts like a profit center. Except for the director of academic & scientific affairs, all the staff is paid by external funding (incomes from different projects). At the end, the balance is close to zero.

The main actors which are in the business process are: the client, the customer, the contractor, the project manager, the project team, the suppliers and the stakeholders.

A.4 Sample projects

CSL electronics laboratory is the offspring of the electronics lab at the Liege University Institute of Astrophysics. Before the start of space exploration, the center were already busy with low light level measurement, spectrometry, light sensors and amplifiers. As a research institute, CSL is frequently designing and building instruments up to the prototype or qualification level, while the final flight hardware assembly is entrusted to industry. Some sample projects are described below, with emphasis on analog and signal processing aspects.

CLS (Proba 3)

Development of an optical metrology system for Proba3 (formation flying demonstrator) including a pulsed high power laser diode. The challenge included supplying short high power pulses to the laser, current regulation, and drawing constant power from the satellite 28V bus.

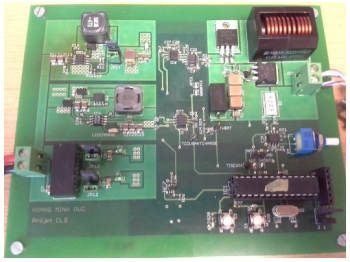

CLS - ESA Project

CRP (Ariane 5)

CRP - Industrial Project

Contactless position sensor for Ariane 5 launcher, including magnetics, EMC and reliability assurance. The device detects the presence of a metal target inside a high pressure enclosure, not needing active electronics inside or holes through the wall. A mixed signal ASIC was designed and a prototype batch was built before handing over to industry.

PACS (Herschel)

CSL designed the complete electronics unit for the mechanisms and detectors of the PACS instrument on board Herschel Space Observatory. Part of the work was driving a cryogenic motor for the wavelength selection grating. The motor is a 2 phase brushless DC design with Hall effect sensors, and the grating position is measured by a synchro/resolver. CSL designed the complete control system including class A low EMI current drivers for the motor coils, A/D conversion electronics and digital servo software.

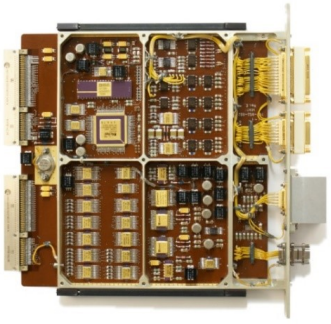

PACS - ESA Project

ESIO instrument

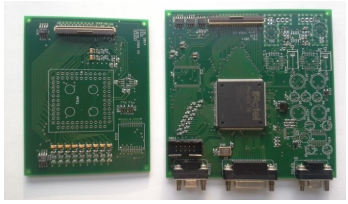

ESIO - ESA Project

Study and breadboarding of a space weather payload. An instrument component is the flux monitor. CSL designed and built the photometry chain, comprising UV sensitive photodiode, transconductance amplifier, gain stage, filtering and A/D conversion. A prototype was built within a cubesat form factor.

WRTF (JUICE)

The Wide Range Thermal Facility is designed to test material samples and solar panels for a Jupiter mission. The CSL electronics lab designed and built the facility monitoring and control, including a 192 channels heater control rack and a temperature measurement unit for cryogenic diodes sensors. Each acquisition board can manage up to 12 sensors. The measurement accuracy can be as low as 15 mK.

WRTF - JUICE

Appendix B

Op-amp choice

The table B.1 compares op-amps from EPPL and describes the needs of this thesis.

Amplifier	**RailtoRail**	**Vcc**	**Vid**	**Vin**	**Vos**	**Ib**
RHF200K-01V	no	5V	1,6 to Vcc -1,5	0 to Vcc	+/-10mV	0,15uA
RHF330K-01V	no	5V	+/-0,5V	+/-2,5V	+/-3,1mV	55uA
RHF310K-01V	no	5V	+/-0,5V	+/-2,5V	+/-6,5mV	15uA
LM124AW	no	32Vmax	32V	-0,3V - 32V	+/-4mV	-100nA
OP27A	no	+/-15V		+/-Vcc	10uV	+/-10nA
OP470A	no	+/-15V	+/-1V	Vcc	0,1mV	6nA
RHF484K-01V	yes	4V to 14V	+/-1,2V	(Vcc-) -0,3V to Vcc+0,3V	60uV	6nA
RHR61K01V	yes	5V	+/-Vcc	(Vcc-) - 0,2V to Vcc+ +0,2V	3mV	1pA
RHR64K01V	yes	5V	+/-Vcc	(Vcc-) - 0,2V to Vcc+ +0,2V	3mV	1pA
RHF43B	yes	3V to 16V	+/-1,2V	(Vcc-) -0,3 to 16V	100uV	30nA
RHF350K-01V	no	5V	+/-0,5V	+/-2,5V	1mV	9uA
OP77	no	+/-22Vmax	+/-30V	+/-Vcc	20uV	2,4nA
AD8001	no	+/-5V	+/-1,2V	+/-Vcc	2mV	5uA
Peltier controller						
Pin current source		5V	0 to 5V	0 to 5V		
Buffer		5V	746mV max	526 to 746mV		
Error		+5/-5V	+/-150mV	526 to 746mV		
PID		+5/-5V	+/-150mV	+/-150mV		
Summer		+5/-5V	+/-450mV	+/-450mV		
Inverter		5V	+/-4,5V	+/-4,5V		
Current source Peltier		+12V	0 to 12V	0 to 12V		
Source controller						
Pin current source		5V	0 to 5V	0 to 5V		
Preamplifier		5V	0 to 100mV	0 to 100mV		
Schmitt trigger		12V	0 to 2V	0 to 4,5V		
Ouput		5V	0 to 5V	0 to 5V		

Table B.1 – Op-amp comparative table

Appendix C

Complete schematics

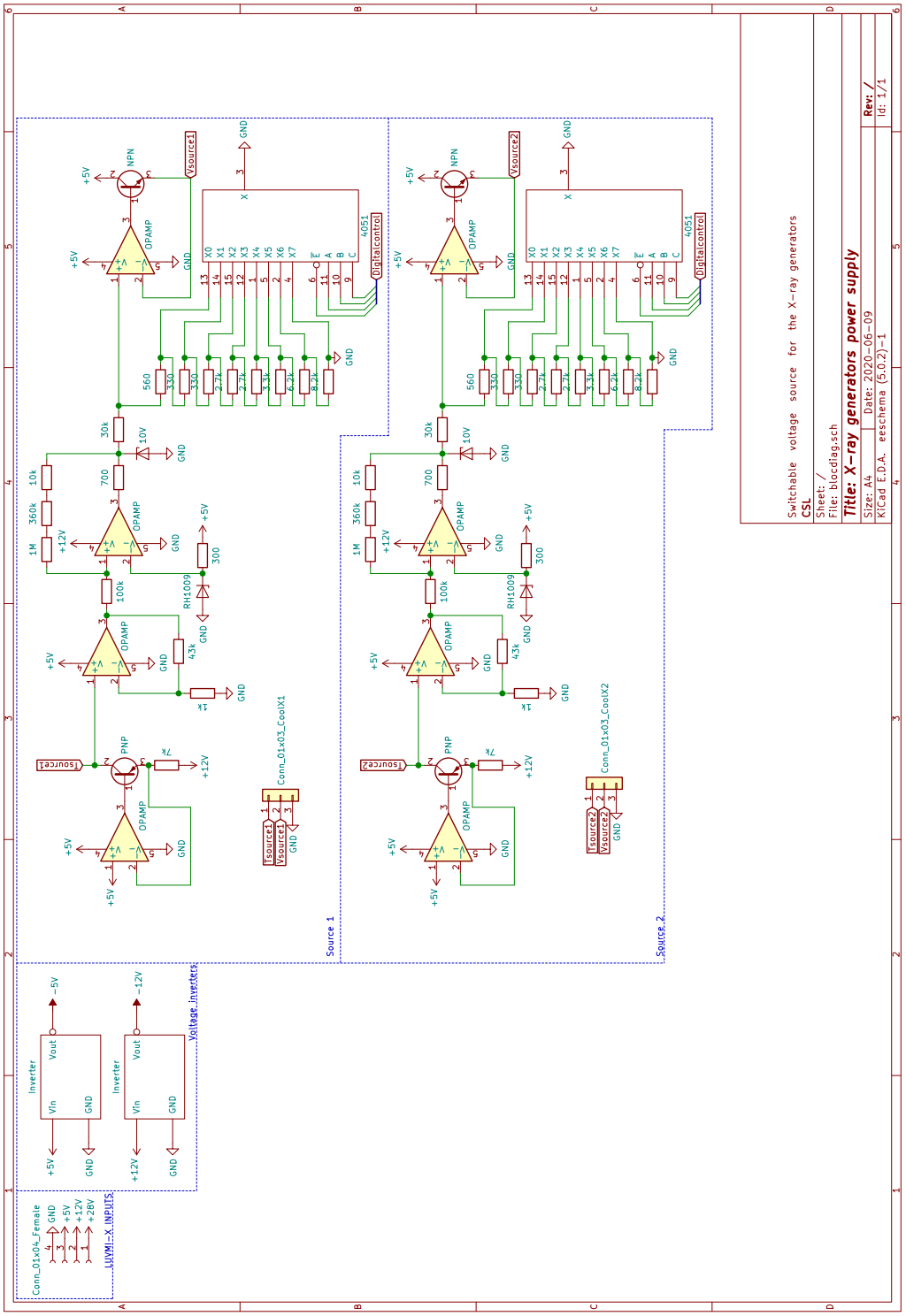

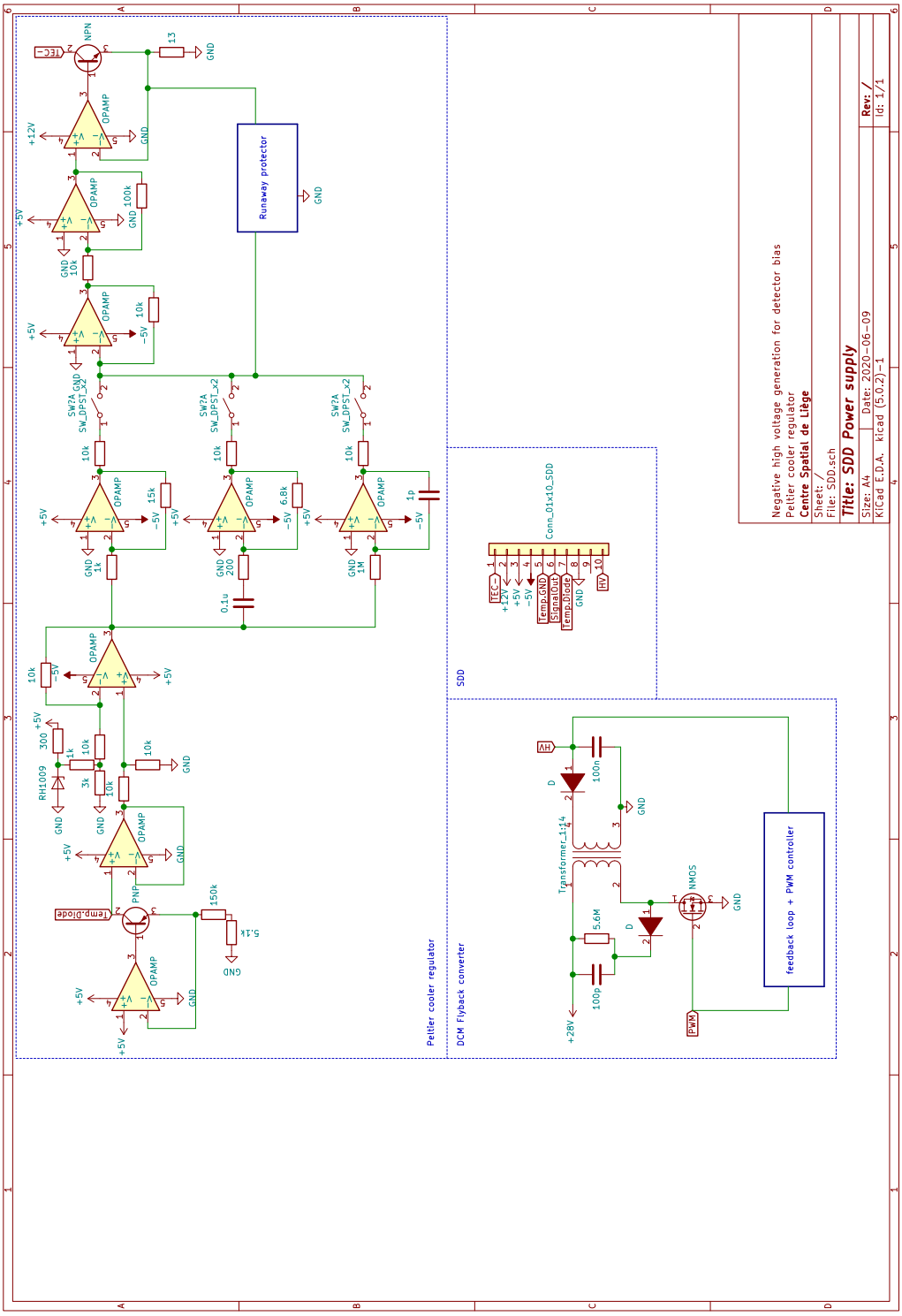
Negative high voltage generation for detector bias
Peltier cooler regulator
Centre Spatial de Liège
Sheet: /
File: SDD.sch
Title: SDD Power supply
Size: A4
Date: 2020-06-09
KiCad E.D.A. kicad (5.0.2)-1
Rev: /
Id: 1/1
Runaway protector
Peltier cooler regulator
SDD
DCM Flyback converter
feedback loop + PWM controller
Conn_01x10_SDD
Transformer_1:1:4
NPN
PNP
NMOS
OPAMP
SW_DPST_x2
RH1009
Temp_Diode
TEC-
HV
PWM
GND
+5V
+12V
-5V
+26V

Appendix D

Excel table to compute flyback values

Input spec	
Vin_nom [V]	28
Vin_min [V]	16
Vin_max [V]	36

Regulator spec	
fsw [Hz]	5E+05
Dmax	0,5

Output spec	
Vout_nom [V]	225
Vout_min [V]	220
Vout_max [V]	230
Iout_max [A]	1E-04
Vrpl_max [V]	5E-03
Efficiency	1

Design values	
VR [V] at DCM-CCM boundary	16
Pout_max [W]	2E-02
Pin_max [W]	0,023
Ip [A]	5,75E-03
Lp_max [H]	2,78E-03
n	14,1
Is [A]	4,08E-04
Ls_max [H]	5,54E-01
Np_min	1,07E-05
Ip_rms [A]	2,35E-03
Is_rms [A]	1,66E-04
Np	2
Ns	28

Diode	
Vd [V]	0,7
VRVd [V]	729
Irms [A]	1,66E-04

Mosfet	
Vds [V]	800

Output Capacitor		
Zc_max [ohm]	12,3	at fsw
C_min [F]	4E-08	
Irms [A]	1,33E-04	

Core spec	
Core size	EE8,8
Ae [cm²]	5
Bmax [T]	0,3
lm [cm]	15,6
beta	2,6
Kfe	40
Wa [cm²]	6,6
MLT [cm]	11,6

Wire spec	
Ku	0,4
rho [ohm m]	1,68E-08

Primary turn optimization	
np_opt	2
Bac [T]	1,6E-06
Pfe [W]	2,66E-12
alpha1	0,5
alpha2	0,5
Aw1 [cm²]	0,66
Aw2 [cm²]	0,047
R1 [ohm]	5,91E-05
R2 [ohm]	0,012
Pcu1 [W]	3,25E-10
Pcu2 [W]	3,25E-10
Pcu [W]	6,51E-10
Ptot [W]	6,53E-10

-> Solver:	Obj:	min H26
	Contr:	H11 = entier
		$H11$ >= $B24$
	Res:	Evolutionnaire

Snubber Design	
Lleak [H]	8,35E-05
Pleak [W]	6,9E-04
Vs [V]	624
Rclamp [ohm]	5,64E+08
Cclamp_min [F]	3,54E-15